Space Weather

RESEARCH ARTICLE
10.1029/2020SW002654

CME Magnetic Structure and IMF Preconditioning Affecting SEP Transport

Erika Palmerio[1,2,3], Emilia K. J. Kilpua[1], Olivier Witasse[4], David Barnes[5], Beatriz Sánchez-Cano[6], Andreas J. Weiss[7,8,9], Teresa Nieves-Chinchilla[10], Christian Möstl[7,9], Lan K. Jian[10], Marilena Mierla[11,12], Andrei N. Zhukov[11,13], Jingnan Guo[14,15], Luciano Rodriguez[11], Patrick J. Lowrance[16], Alexey Isavnin[17], Lucile Turc[1], Yoshifumi Futaana[18], and Mats Holmström[18]

[1]Department of Physics, University of Helsinki, Helsinki, Finland, [2]Space Sciences Laboratory, University of California–Berkeley, Berkeley, CA, USA, [3]CPAESS, University Corporation for Atmospheric Research, Boulder, CO, USA, [4]ESTEC, European Space Agency, Noordwijk, the Netherlands, [5]STFC RAL Space, Rutherford Appleton Laboratory, Harwell Campus, Oxfordshire, UK, [6]School of Physics and Astronomy, University of Leicester, Leicester, UK, [7]Space Research Institute, Austrian Academy of Sciences, Graz, Austria, [8]Institute of Physics, University of Graz, Graz, Austria, [9]Institute of Geodesy, Graz University of Technology, Graz, Austria, [10]NASA Goddard Space Flight Center, Heliophysics Science Division, Greenbelt, MD, USA, [11]Solar–Terrestrial Centre of Excellence—SIDC, Royal Observatory of Belgium, Brussels, Belgium, [12]Institute of Geodynamics of the Romanian Academy, Bucharest, Romania, [13]Skobeltsyn Institute of Nuclear Physics, Moscow State University, Moscow, Russia, [14]School of Earth and Space Sciences, University of Science and Technology of China, Hefei, China, [15]CAS Center for Excellence in Comparative Planetology, University of Science and Technology of China, Hefei, China, [16]IPAC–Spitzer, California Institute of Technology, Pasadena, CA, USA, [17]Rays of Space Oy, Vantaa, Finland, [18]Swedish Institute of Space Physics, Kiruna, Sweden

Key Points:

- We analyze the May 11, 2012 coronal mass ejections (CME) and the May 17, 2012 solar energetic particle (SEP) event through the inner heliosphere
- The May 11 CME appeared to rotate rapidly upon eruption and then considerably during its interplanetary propagation
- The May 11 CME provided direct magnetic connectivity for the efficient transport of SEPs from the May 17 event

Supporting Information:

Supporting Information may be found in the online version of this article.

Correspondence to:

E. Palmerio,
epalmerio@berkeley.edu

Citation:

Palmerio, E., Kilpua, E. K. J., Witasse, O., Barnes, D., Sánchez-Cano, B., Weiss, A. J., et al. (2021). CME magnetic structure and IMF preconditioning affecting SEP transport. *Space Weather*, *19*, e2020SW002654. https://doi.org/10.1029/2020SW002654

Received 9 OCT 2020
Accepted 1 FEB 2021

Abstract Coronal mass ejections (CMEs) and solar energetic particles (SEPs) are two phenomena that can cause severe space weather effects throughout the heliosphere. The evolution of CMEs, especially in terms of their magnetic structure, and the configuration of the interplanetary magnetic field (IMF) that influences the transport of SEPs are currently areas of active research. These two aspects are not necessarily independent of each other, especially during solar maximum when multiple eruptive events can occur close in time. Accordingly, we present the analysis of a CME that erupted on May 11, 2012 (SOL2012-05-11) and an SEP event following an eruption that took place on May 17, 2012 (SOL2012-05-17). After observing the May 11 CME using remote-sensing data from three viewpoints, we evaluate its propagation through interplanetary space using several models. Then, we analyze in-situ measurements from five predicted impact locations (Venus, Earth, the Spitzer Space Telescope, the Mars Science Laboratory en route to Mars, and Mars) in order to search for CME signatures. We find that all in-situ locations detect signatures of an SEP event, which we trace back to the May 17 eruption. These findings suggest that the May 11 CME provided a direct magnetic connectivity for the efficient transport of SEPs. We discuss the space weather implications of CME evolution, regarding in particular its magnetic structure, and CME-driven IMF preconditioning that facilitates SEP transport. Finally, this work remarks the importance of using data from multiple spacecraft, even those that do not include space weather research as their primary objective.

1. Introduction

Solar energetic particle (SEP; e.g., Reames, 2015; Vainio et al., 2009) events are increases in high-energy particle fluxes with energies in the keV–GeV range lasting from hours to days and important drivers of space weather effects (e.g., Koskinen et al., 2017). They are intrinsically related to two major classes of eruptions from the Sun, namely flares (e.g., Benz, 2017) and coronal mass ejections (CMEs; e.g., Webb & Howard, 2012). These phenomena can take place either together or separately in the solar atmosphere, and both can contribute to the production of SEPs, although in different but yet connected ways. Explosive magnetic reconnection during solar flares can accelerate particles, which then travel along the interplanetary magnetic field (IMF; e.g., Owens & Forsyth, 2013) lines connecting to an observer. CMEs, on the other hand, consist of copious amounts of plasma and magnetic field that are released into interplanetary space and that can drive shock waves, thus acting as efficient particle accelerators. Contrarily to flares that accelerate particles only on the solar surface, CME-driven shocks may accelerate particles locally in the low corona and also

at large distances in the heliosphere, with acceleration sites that typically extend much wider. These two forms of SEP production have traditionally resulted in a clear distinction of particle acceleration processes (e.g., Cane et al., 1986; Reames, 2013; Vlahos et al., 2019) into flare-accelerated (often with an impulsive profile; e.g., Reames, 1990) and shock-accelerated (more likely to show a gradual time evolution; e.g., Desai & Giacalone, 2016). This "dual nature" of SEPs, however, is not fully representative of the complex nature and interplay of processes that result in particle injection and acceleration, given that different mechanisms can contribute to a single event (e.g., Anastasiadis et al., 2019; Cane et al., 2010).

Since SEPs are accelerated and can propagate more efficiently along magnetic field lines, their spatial distribution is, at least in principle, supposed to be limited to the heliolongitudes (and latitudes) that are magnetically connected to the acceleration site(s) (e.g., Reames, 1999). As a result, impulsive SEP events are expected to be observed predominantly within a narrower region compared to gradual ones (e.g., Reames, 2002, 2013). Nevertheless, surprisingly wide (i.e., significantly larger than a flare site or a CME-driven shock front) longitudinal distributions of SEPs have been reported for both impulsive (e.g., Lario et al., 2017; Wibberenz & Cane, 2006; Wiedenbeck et al., 2013) and gradual (e.g., Dresing et al., 2012; Richardson et al., 2014; Rouillard et al., 2012) events. Possible reasons for wide-spread SEP distributions are cross-field transport in the interplanetary medium and/or an extended source region at the Sun injecting particles over a broad region (e.g., Dresing et al., 2014). Accordingly, from a space weather perspective, current SEP research focuses not only on how intense an event could be, but also on which heliolongitudes it could extend to (see, e.g., the recent reviews by Klein & Dalla, 2017; Malandraki & Crosby, 2018).

Being large-scale magnetic disturbances, CMEs profoundly affect the structure of the IMF during their journey away from the Sun (e.g., Witasse et al., 2017). As a result, the passage of a CME may provide a temporary magnetic connection between two regions in the heliosphere that would otherwise not be linked. This may result in energetic particles observed in situ "inside" an interplanetary CME (or ICME; e.g., Kilpua et al., 2017) that preceded the SEP event (e.g., Dresing et al., 2016; Larson et al., 1997; Masson et al., 2012; Rodriguez et al., 2008). In these efforts, knowledge of the magnetic structure of CMEs in interplanetary space is crucial. Regardless of their pre-eruptive magnetic configuration, it is generally agreed that all CMEs lift off from the Sun as helical magnetic structures called flux ropes (e.g., Forbes, 2000; Green et al., 2018; Vourlidas et al., 2013), which consist of bundles of magnetic field lines that wind about a common axis. From a space weather perspective, there are several factors to take into account after a CME has left the Sun, that is, its size and propagation direction, which determine whether a CME will impact a certain location (e.g., Mays et al., 2015; Möstl et al., 2017; Rodriguez et al., 2011), its propagation speed, which determines the arrival time (e.g., Verbeke et al., 2019; Zhao & Dryer, 2014), and its magnetic structure, which is important in determining the resulting space weather response (e.g., Kilpua, Lugaz, et al., 2019; Savani et al., 2015). A review summarizing the current status of space weather forecasting of CMEs has been recently published by Vourlidas et al. (2019). While hit/miss and arrival time predictions presently lie around a hit rate of ∼0.5 and an accuracy of ±10 h (e.g., Riley et al., 2018; Wold et al., 2018), current models can only reproduce, rather than effectively forecast, the magnetic structure of CMEs. This is because, even if the magnetic configuration of flux ropes during eruption can be indirectly estimated from remote-sensing observations (e.g., Gopalswamy et al., 2018; Palmerio et al., 2017), it can differ significantly when measured in situ (e.g., Palmerio et al., 2018; Yurchyshyn, 2008). Parameters that can influence the evolution of CMEs as they travel away from the Sun are , for example, deflections (e.g., Kay et al., 2015; Wang et al., 2004; Zhuang et al., 2017), rotations (e.g., Isavnin et al., 2013; Kliem et al., 2012; Vourlidas et al., 2011), deformations (e.g., Manchester et al., 2004; Owens, 2008; Savani et al., 2010), and interactions with the ambient solar wind (e.g., Rodriguez et al., 2016; Rouillard et al., 2010; Winslow et al., 2016), stream interaction regions (e.g., Heinemann et al., 2019; Y. Liu et al., 2019; Prise et al., 2015), and/or with other CMEs (e.g., Kilpua, Good, et al., 2019; Lugaz & Farrugia, 2014; Scolini et al., 2020). Comprehensive reviews on the interplanetary evolution of CMEs have been recently published by Lugaz et al. (2017), Luhmann et al. (2020), and Manchester et al. (2017).

In this work, we explore the large-scale preconditioning of the IMF resulting from the passage of an ICME and its subsequent effects on the transport of SEPs. We study the eruption and interplanetary evolution of a CME that erupted on May 11, 2012 with a particular focus on its magnetic structure as it travels away from the Sun. We evaluate the propagation of the CME across the inner heliosphere and how its orientation

changed, indicating that the flux rope rotated and was distorted significantly after erupting. Furthermore, we analyze the SEP event following the May 17, 2012 eruption, which was observed in situ at eight well-separated locations in the inner heliosphere, including all four planets therein: Mercury, Venus, Earth, and Mars. We show that five of the eight available observers recorded a nearly simultaneous SEP event characterized by an impulsive profile, while the remaining three observed a more gradual event. These findings are consistent with the IMF being affected by the passage of an ICME, since impulsive SEP profiles were observed at those locations that were predicted to be encountered by the May 11 CME. We suggest that the ICME provided the required "direct" magnetic connectivity for SEPs to spread rapidly over a broad region (the observing locations engulf over ∼0.9 AU in radial distance and $\sim 70^{r}c$ in longitude, extending up to ∼150° in longitude away from the flaring site). The May 17, 2012 SEP event was studied extensively in the literature, especially between the Sun and Earth, but, to our knowledge, this is the first report of its observations at eight different locations, five of which were impacted by a preceding ICME.

This article is organized as follows. In Section 2, we enumerate the space- and ground-based instruments that are employed in this study. In Section 3, we describe the two eruptive events under analysis (May 11 and May 17, 2012) from a remote-sensing observational perspective. In Section 4, we estimate the propagation of the May 11 CME and its impact at different locations using several models. In Section 5, we present the in-situ signatures of the May 11 CME and May 17 SEP event across the inner heliosphere. In Section 6, we discuss various aspects of the evolution of the May 11 CME in terms of its propagation, its magnetic structure, and its role in the transport of SEPs, by combining observational data with modeling outputs. Finally, in Section 7, we conclude by summarizing our results.

2. Spacecraft and Ground-Based Data

In this section, we list the fleet of instruments that are involved in this study, in the order in which they are introduced in this article. We use a synthesis of remote-sensing and in-situ data in order to follow and observe signatures of the May 11, 2012 CME and the May 17, 2012 SEP event at different locations throughout the inner heliosphere.

Solar observations from Earth's viewpoint are made with the Solar Dynamics Observatory (SDO; Pesnell et al., 2012). The extreme ultra-violet (EUV) images and line-of-sight magnetograms we use are taken with the Atmospheric Imaging Assembly (AIA; Lemen et al., 2012) and the Helioseismic and Magnetic Imager (HMI; Scherrer et al., 2012), respectively. Solar observations from other locations at ∼1 AU are made with the Sun Earth Connection Coronal and Heliospheric Investigation (SECCHI; R. A. Howard et al., 2008) Extreme UltraViolet Imager (EUVI) onboard the Solar Terrestrial Relations Observatory (STEREO; Kaiser et al., 2008). STEREO consists of twin spacecraft that orbit the Sun, one ahead of Earth in its orbit (STEREO-A) and the other one trailing behind (STEREO-B, which has been out of contact since October 2014). Furthermore, we use data from the X-ray Sensor (XRS) onboard the Geostationary Operational Environmental Satellites (GOES) 15 satellite to study the solar X-ray flux.

Coronagraph observations are also made from three vantage points. The view from Earth is provided by the Large Angle and Spectrometric Coronagraph (LASCO; Brueckner et al., 1995) C2 (2.2–6 $R_{\odot}$) and C3 (3.5–30 $R_{\odot}$) instruments onboard the Solar and Heliospheric Observatory (SOHO: Domingo et al., 1995). The views from STEREO-A and STEREO-B are provided by the SECCHI/COR1 (1.5–4 $R_{\odot}$) and COR2 (2.5–15 $R_{\odot}$) coronagraphs.

Heliospheric observations are made with the Heliospheric Imagers (HI; Eyles et al., 2009) onboard the twin STEREO spacecraft. Each HI instrument comprises two cameras, HI1 (4–24°) and HI2 (18–88°), that image the space between the Sun and Earth (the degrees measure the elongation in helioprojective radial coordinates).

In-situ measurements around Venus are taken with Venus Express (VEX; Svedhem et al., 2007). We use data from the Magnetometer (MAG; Zhang et al., 2006) and the Analyser of Space Plasmas and Energetic Atoms (ASPERA-4; Barabash et al., 2007). The sensors that we use from ASPERA-4 are the Ion Mass Analyser (IMA) and the Electron Spectrometer (ELS), both performing local charged particle measurements. VEX, which ended its operations in 2015, had a 24-h highly elliptical and quasipolar orbit, and spent a couple of

hours each day inside the induced magnetosphere of Venus. ASPERA-4 was operational for several hours close to periapsis and apoapsis only, while the magnetometer ran continuously.

In-situ measurements from near Earth are mainly taken with the Wind satellite, which is operational at Earth's Lagrange L1 point. We use data from the Magnetic Fields Investigation (MFI; Lepping et al., 1995) and Solar Wind Experiment (SWE; Ogilvie et al., 1995) instruments, which measure magnetic field and plasma (including solar wind electron distributions) continuously. Additionally, we use proton flux data from the Electron, Proton, and Alpha Detector (EPEAD) instrument onboard GOES-13. We also study variations in cosmic rays and SEPs on the ground using count rate data from the Neutron Monitor Database (NMDB), and in particular from the South Pole (SOPO) neutron monitor.

Measurements around 1 AU are also taken with the Spitzer Space Telescope (Werner et al., 2004), which orbits the Sun on an Earth-trailing orbit. In order to evaluate the impact of space weather events at Spitzer, we count the radiation hits on the Infrared Array Camera (IRAC; Fazio et al., 2004). Spitzer was deactivated in 2020.

We also analyze data recorded by the Mars Science Laboratory (MSL; Grotzinger et al., 2012) spacecraft that was en route to Mars at the time of this study. We use data from the Radiation Assessment Detector (RAD; Hassler et al., 2012) instrument onboard the Curiosity rover, and in particular from the plastic scintillator "E," which measures the radiation dose rate contributed by all particles reaching the detector from all directions and provides the best statistics of background cosmic ray fluxes.

In-situ measurements from Mars are taken with two different spacecraft. The first is Mars Express (MEX; Chicarro et al., 2004). We use data from the Mars Advanced Radar for Subsurface and Ionospheric Sounding (MARSIS; Picardi et al., 2004) and the Analyzer of Space Plasmas and Energetic Atoms (ASPERA-3; Barabash et al., 2006). MARSIS is a high-frequency sounding radar dedicated to probe the Martian subsurface, surface, and ionosphere. ASPERA-3 is identical to the ASPERA-4 instrument onboard VEX, and the sensors that we use are again IMA and ELS. MEX has a 7-h elliptical orbit, with a periapsis distance of ∼300 km and an apoapsis distance of ∼10,000 km from the planet's surface. MARSIS takes measurements at periapsis only, while ASPERA-3 was operational for about half of the orbit during the time of the events under study. The second satellite is 2001 Mars Odyssey (MOdy; Saunders et al., 2004), from which we use data taken with the High Energy Neutron Detector (HEND), which is part of the Gamma Ray Spectrometer (GRS; Boynton et al., 2004) suite.

Finally, we inspect SEP measurements made at the twin STEREO spacecraft and Mercury. At STEREO, we use data from the High Energy Telescope (HET; von Rosenvinge et al., 2008), which is part of the In situ Measurements of Particles And CME Transients (IMPACT; Luhmann et al., 2008) investigation. At Mercury, we use data from the Mercury Surface, Space Environment, Geochemistry, and Ranging (MESSENGER; Solomon et al., 2007) spacecraft, which orbited the innermost planet between 2011 and 2015. We examine measurements taken with the Neutron Spectrometer (NS) sensor, part of the Gamma-Ray and Neutron Spectrometer (GRNS; Goldsten et al., 2007) instrument and dedicated to measuring the flux of ejected neutrons.

3. Remote-Sensing Observations

In this section, we describe the eruptive events of May 11, 2012 (Section 3.1) and May 17 (Section 3.2) from a remote-sensing observational perspective. The positions of the inner planets and the spacecraft employed in this study, together with the eruptions' source region locations at the Sun, are shown in Figure 1 for (a) May 11 and (b) May 17.

3.1. The May 11, 2012 Eruption

The first eruptive event that we focus on in this work initiated from a small active region containing a filament on May 11, 2012 around 23:00 UT. In this section, we follow the eruption and subsequent propagation of the associated large-scale CME using remote-sensing observations of the solar disc, the solar corona, and the heliosphere.

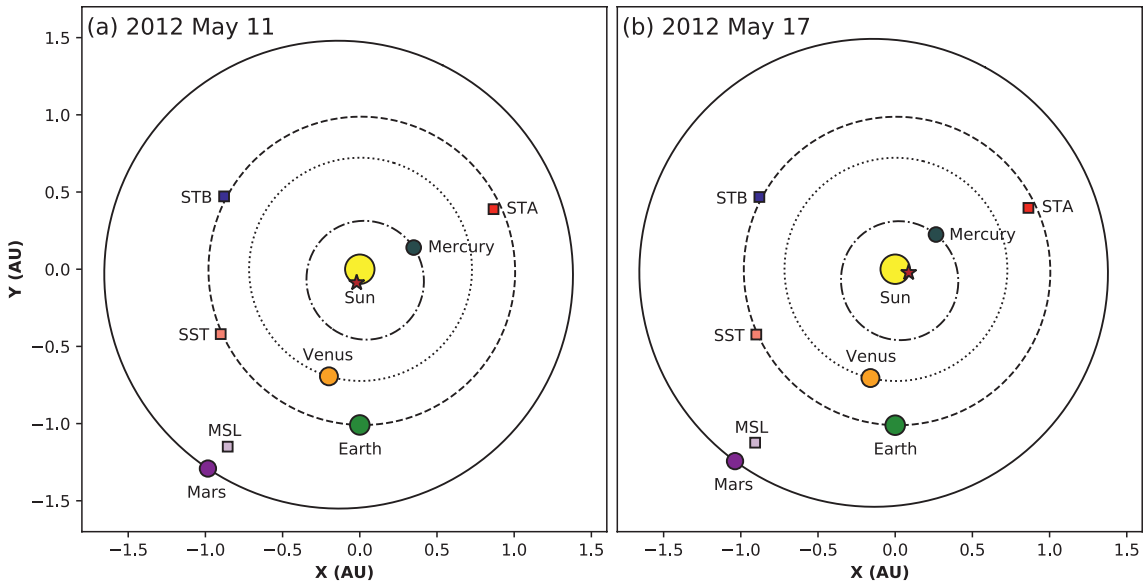

Figure 1. Position of various planets and spacecraft in the inner solar system (i.e., up to Mars' orbit) on (a) May 11, 2012 and (b) May 17, 2012 projected onto the solar equatorial plane. The projected source locations of the May 11 and May 17 eruptions are indicated by a star symbol on the surface of the Sun in panels (a and b), respectively. The planets are marked with circles, while the spacecraft are marked with squares (STA = STEREO-A; STB = STEREO-B; SST = Spitzer Space Telescope; MSL = Mars Science Laboratory). The orbits of all planets are also indicated.

3.1.1. Solar Disc Observations

The active region from which the May 11, 2012 CME originated appeared on the eastern limb of the Earth-facing Sun on May 6, 2012 on the southern hemisphere. It was not attributed a National Oceanic and Atmospheric Administration (NOAA) classification number, but it had Space-weather HMI Active Region Patch (SHARP; Bobra et al., 2014) number 1642. An S-shaped filament was clearly visible within the active region throughout its rotation toward the central meridian. The filament erupted on May 11, 2012 around 23:00 UT, from approximately S13E13. The top panels of Figure 2 show the evolution of the eruption process in remote-sensing data from SDO's perspective. For the complete set of observations of the erupting filament from three viewpoints (STEREO-A, SDO, and STEREO-B), see Movie S1.

The magnetic structure of the flux rope associated with the erupting CME, or intrinsic flux rope type, can be estimated using a combination of several indirect proxies at different wavelengths in remote-sensing data of the solar disc (for a summary of the proxies that can be used to determine chirality, tilt, and field direction at the axis of a flux rope, see Palmerio et al., 2017). In the particular case under study, we note that the forward S-shape of the erupting filament (Figure 2a) is a sign of right-handed chirality (e.g., Martin et al., 2012). Furthermore, the forward J-shape of the flare ribbons associated with the eruption (bright features in Figures 2b and 2c) confirms the right-handedness of the flux rope (e.g., Démoulin et al., 1996). We infer the tilt of the flux rope axis by taking the average inclination between the polarity inversion line (PIL) and post-eruption arcades (PEAs). We determine the tilt of the flux rope to be ∼65° with respect to the solar equator. Finally, we determine the magnetic field direction at the flux rope axis from coronal dimmings, which are believed to map to the CME footpoints (e.g., B. J. Thompson et al., 2000). The dimming regions marked in Figure 2d indicate that the axial field was directed roughly toward the south at the time of the eruption. Thus, we determine the intrinsic flux rope type of the CME under study to be right-handed with a mostly southward axial field, or east–south–west (ESW) according to the convention of Bothmer and Schwenn (1998) and Mulligan et al. (1998).

Upon eruption, the filament spine was seen to rotate clearly clockwise (Figures 2a–2c), as expected for a right-handed flux rope (e.g., Fan & Gibson, 2004; Green et al., 2007; Lynch et al., 2009). Its southern leg (i.e., the eastern leg upon rotation) could no longer be seen in SDO images shortly after the eruption, while its northern leg (i.e., the western leg upon rotation) could be observed for a couple of hours after the eruption onset. STEREO-B observations (see Movie S1), taken from an almost-quadrature view with respect to SDO,

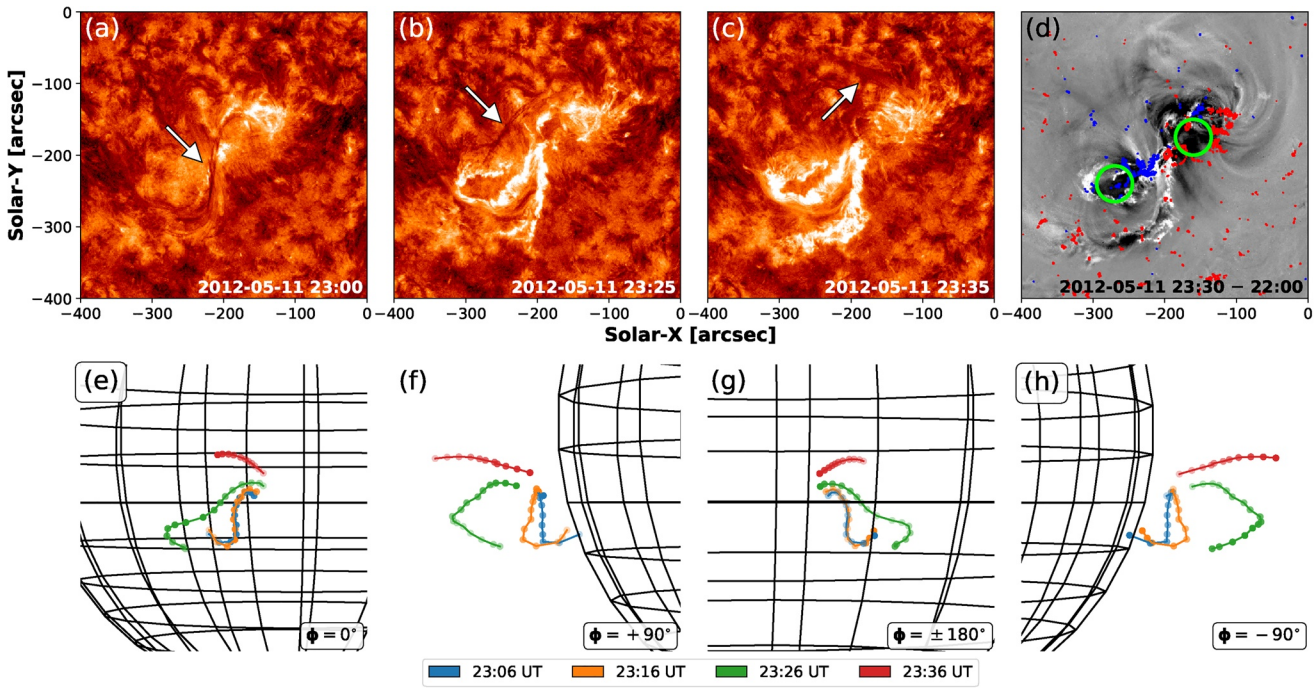

Figure 2. The May 11, 2012 eruption from solar disc data. (a–c) The erupting filament as seen by SDO/AIA in the 304 Å channel, with the rotating filament indicated by an arrow in each panel. (d) Base-difference image taken with SDO/AIA in the 211 Å channel and overlaid with SDO/HMI magnetogram contours (blue = negative polarity, red = positive polarity). The dimming regions (signatures of the flux rope footpoints) have been circled in green. (e–h) The erupting filament triangulated with the tie-pointing technique using SDO/AIA and STEREO/SECCHI/EUVI-B data in the 304 Å channel. The same reconstruction is shown from four different longitudinal perspectives (indicated in each panel in Stonyhurst coordinates; W. T. Thompson, 2006) to facilitate its 3D visualization. Each color represents one different timestamp within the same panel. AIA, Atmospheric Imaging Assembly; EUV, extreme ultra-violet; HMI, Helioseismic and Magnetic Imager; SDO, Solar Dynamics Observatory.

show that the southeastern leg of the filament appeared to disconnect from the Sun approximately at the time of its disappearance in SDO imagery. Such asymmetric filament eruptions have been observed in previous studies (e.g., Liu et al. 2009; Tripathi et al., 2006). According to the definition of R. Liu et al. (2009), the filament eruption studied here can be classified as whipping-like, where the filament "active" leg whips upwards and the "anchored" leg remains fixed to the photosphere. In such a scenario, the mass in the active leg could either fall back toward the Sun or fail to follow the motion of the filament spine, thus showing an apparent detachment of the leg from the solar surface, to which the filament field may however still be connected. Another possibility is that the active leg undergoes interchange reconnection with a nearby coronal hole open field (e.g., Baker et al., 2009; Zhu et al., 2014), hence opening one end of the filament to interplanetary space. In the event studied here, the motion of the flare ribbon brightenings to the south of the CME source region (visible in Figures 2b and 2c and in Movie S1), corresponding to the extent of a small region of open field (visible in SDO/AIA 193 Å imagery, data not shown), supports this latter scenario.

The bottom panels of Figure 2 show 3D reconstructions of the filament during the early phase of its eruption using the tie-pointing triangulation technique. The method was first employed by W. T. Thompson (2009) to triangulate a Sun-grazing comet, but it has been used since then also to evaluate the 3D rotation of erupting filaments (e.g., Bemporad et al., 2011; W. T. Thompson et al., 2012). The reconstructions presented here are obtained using SDO/AIA and STEREO/SECCHI/EUVI-B data, both in the 304 Å channel. At the fourth and last triangulation (23:36 UT), the southeastern (active) leg of the filament had completely disappeared, hence we could only triangulate the northwestern (anchored) one. It should be emphasized that erupting filaments are thick in EUV images and the resulting triangulated structures are expected to be accompanied by significant uncertainties. Consequently, the resulting structures shown in Figures 2e–2h should be considered only as approximate indicators of the global 3D shape of the erupting filament. Nevertheless, regardless of the connection of the active filament leg to the Sun, the observations reported here suggest that the filament changed its orientation from a roughly perpendicular to a roughly parallel one with respect

to the solar equator, rotating by ∼85° clockwise. Whether the associated flux rope experienced the same evolution, however, is unclear, as the spatial relationship between erupting filaments and the overlying flux rope is an open question (e.g., Gibson et al., 2006; Vourlidas et al., 2013). If we assume that the orientation of a flux rope follows that of its corresponding filament, we can deduce that the flux rope type changed from ESW to north–east–south (NES) due to such rotation.

3.1.2. Coronagraph Observations

After erupting, the May 11, 2012 CME was visible in coronagraphs from three well-separated viewpoints (SOHO, STEREO-A, and STEREO-B) as it propagated through the solar corona (see Movie S2). The CME is seen pointing toward the west in STEREO-B and toward the east in STEREO-A imagery, indicating an Earth-directed eruption. However, we note from SOHO images that the CME propagated slightly eastwards rather that along the Sun–Earth line, indicating that the eruption was directed roughly toward Mars (see the positions of different planets and spacecraft in Figure 1a).

The top two rows of Figure 3 show composite images using EUVI and COR1 data from both STEREO-A (panels a–d) and STEREO-B (panels e–h). In particular, STEREO-B imagery shows that the filament leg that disappeared first as seen from SDO (i.e., the active leg, Figures 2a–2c) rotated significantly from a downward-facing hook (Figure 3e) to an upward-facing hook (Figure 3g) morphology. The western leg appeared to be still attached to the Sun throughout the rotation phase. The corresponding large-scale CME, in turn, featured a single-front structure from the STEREO-A perspective (marked by an arrow in Figures 3b–3d and visible in Movie S2) and a double-bump structured front from the STEREO-B and SOHO viewpoints (marked by arrows in Figures 3f and 3g and visible in Movie S2). We note that asymmetric white-light CMEs associated with whipping-like filament eruptions were reported in previous studies, for example, by Zhu et al. (2014).

The bottom row of Figure 3 shows 3D reconstructions of the filament, performed using the tie-pointing technique on composite EUVI and COR1 images from both STEREO spacecraft, and the overlying large-scale CME, performed using the graduated cylindrical shell (GCS; Thernisien et al., 2006; Thernisien et al., 2009) reconstruction technique on COR1 images from both STEREO spacecraft. The morphology of the GCS model is that of a hollow wireframe, with six free parameters that can be manually adjusted until they best match the data. For the reconstruction shown here, we only include the "main" structure seen in STEREO-B (i.e., that indicated by the top arrow in Figure 3g). According to the resulting 3D images shown in Figures 3i–3l, the western leg of the filament (i.e., the anchored leg discussed in Section 3.1.1) follows the western leg of the larger-scale CME quite closely, and the detachment and slight rotation northwards of the active filament leg are also evident. To the thick nature of filaments discussed in Section 3.1.1, we add that in this case the tie-pointing reconstruction was applied to simultaneous EUV and white-light images, that is using instruments that measure at different wavelengths, resulting in large uncertainties. Nevertheless, considering how well the resulting 3D thread fits within the larger CME structure, these results can be considered a good approximation of the general morphology and relative orientation of the two features. The tilt of the CME inferred from the GCS reconstruction is in this case close to 0°, meaning that the eruption was seen basically edge-on from both STEREO spacecraft. This also implies that it is not possible to determine whether the eastern CME leg, which corresponds to the active filament leg, was still attached to the Sun at this point, either entirely or at least partially. Nevertheless, the low tilt angle inferred from the GCS reconstruction is consistent with the filament rotation (see Section 3.1.1 and Figure 2), suggesting that the flux rope axis roughly followed the orientation of the underlying filament and had a NES orientation in the low corona.

Finally, in order to define the global geometric and kinematic parameters of the 2012 May 11 CME during its journey through the solar corona, we further apply the GCS technique to coronagraph images from all three available spacecraft (i.e., SOHO and the twin STEREO). An example of the resulting GCS reconstructions is shown in Figure 4 (for the full CME kinematics, see Figure S1). Throughout its passage through the coronagraphic fields of view, the CME did not seem to experience significant deflections, featuring a propagation direction of −10° in latitude and −30° in longitude in Stonyhurst coordinates. On the other hand, the CME seemed to continue rotating as it traveled away from the Sun, with its axis inclination resulting from our reconstructions evolving gradually from −10° to −65° (a positive tilt value is defined for counterclockwise rotations) with respect to the solar equatorial plane. Finally, its propagation speed was ∼1,000 kms^{-1}

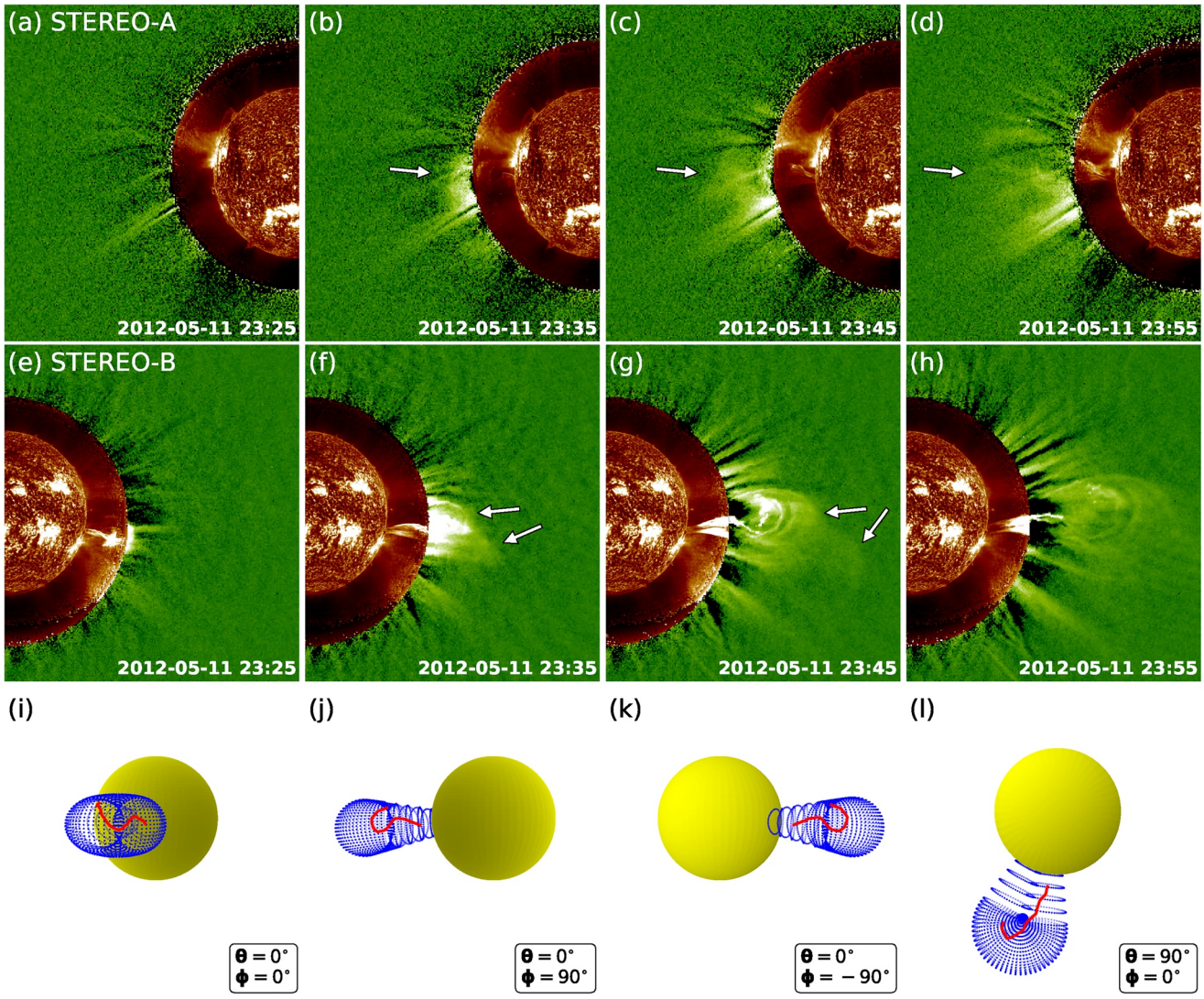

Figure 3. (a–h) Evolution of the erupting filament and the overlying CME (marked by arrows in some of the panels) through the low corona in composite images from STEREO/SECCHI/EUVI in the 304 Å channel and STEREO/SECCHI/COR1 using (a–d) STEREO-A and (e–h) STEREO-B data. The COR1 data are shown as base-difference images, with the background taken at 23:00 UT. (i–l) 3D reconstruction of the erupting filament and the overlying large-scale CME performed at 23:45 UT. The filament (shown in red) is triangulated with the tie-pointing technique using STEREO/SECCHI/EUVI in the 304 Å channel and COR1 composite data from both STEREO spacecraft. The overlying CME (shown as a blue wireframe) is reconstructed with the GCS technique using STEREO/SECCHI/COR1 data from both STEREO spacecraft. The same reconstruction is shown from different perspectives (indicated in each panel in Stonyhurst coordinates) to facilitate its 3D visualisation. CME, coronal mass ejection; EUVI = Extreme UltraViolet Imager; GCS = graduated cylindrical shell; SECCHI, Sun Earth Connection Coronal and Heliospheric Investigation; STEREO, Solar Terrestrial Relations Observatory.

(calculated between successive reconstructions from the CME apex height) throughout the COR2 field of view. However, consisting of a "hollow croissant," the GCS model cannot provide information on the internal magnetic field. Hence, although the handedness of the CME is known from solar disc observations (see Section 3.1.1), the direction of the corresponding flux rope's axial field is characterized by a 180° ambiguity. If we assume that the flux rope followed the same rotation pattern as its associated filament, then it can be concluded that the flux rope axis rotated ~130° from its pre-eruptive configuration to altitudes of a couple tens solar radii. According to these assumptions and minding that the CME was right-handed, it would follow that the flux rope left the outer corona close to a west–north–east (WNE) type, while a 180° reversal of the axis would yield a east–south–west (ESW) type. We remark that, as shown in Figures 3 and 4, and Movie S2, the CME under study appeared highly asymmetric, thus the GCS results should be considered as an approximation of the global orientation of a significantly distorted structure. Furthermore, we note that

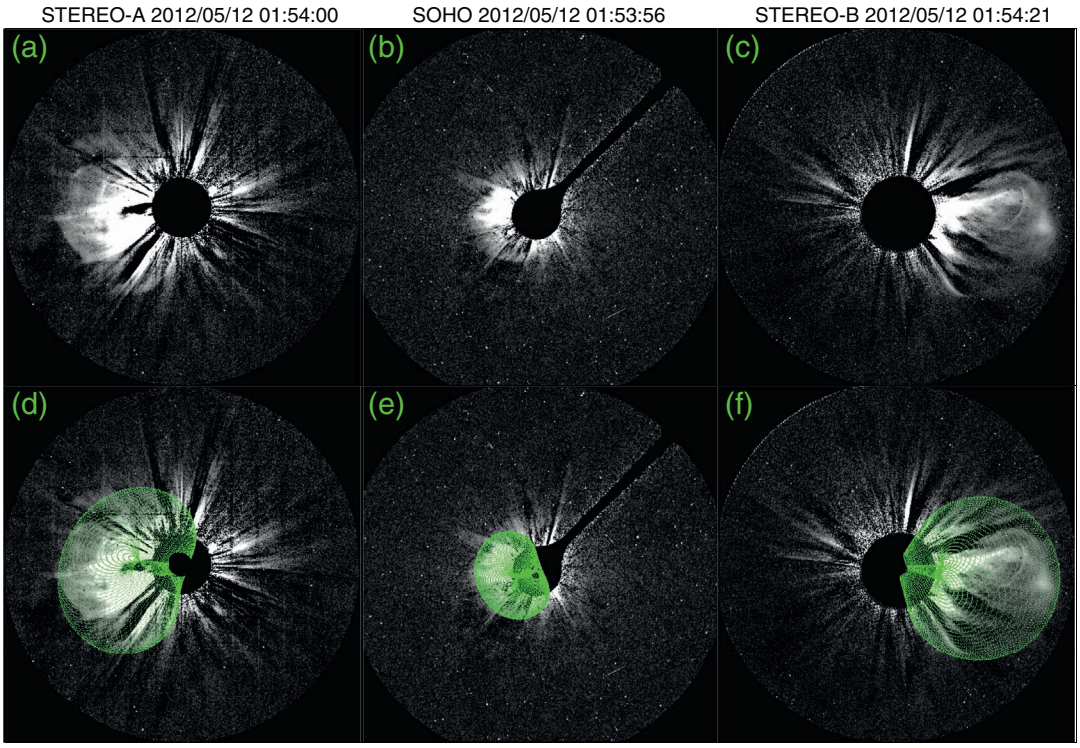

Figure 4. Example of the GCS reconstruction technique applied to the May 11, 2012 CME at the last available time before the CME left the COR2-B field of view (May 12, 2012 01:54 UT). (a–c) Base-difference images taken from STEREO/SECCHI/COR2-A, SOHO/LASCO/C3, and STEREO/SECCHI/COR2-B. (d–f) Same images as in (a–c), with the GCS wireframe overlaid. CME, coronal mass ejection; GCS, graduated cylindrical shell; LASCO, Large Angle and Spectrometric Coronagraph; SECCHI, Sun Earth Connection Coronal and Heliospheric Investigation; SOHO, Solar and Heliospheric Observatory; STEREO, Solar Terrestrial Relations Observatory.

for this event it is particularly difficult to clearly discern the boundaries between the CME itself and the white-light shock driven by it. Hence, being the May 11, 2012 CME far from a "textbook" case, we expect GCS reconstructions to not be able to unequivocally derive the 3D structure of the CME in white light.

3.1.3. HI Observations

After leaving the STEREO/SECCHI/COR2 field of view, the May 11, 2012 CME appeared in the HI cameras onboard both STEREO spacecraft (see Movie S3). Figures 5a and 5b shows a snapshot of the CME as seen in the HI1 field of view. At both spacecraft, observations of the CME in HI1 began at approximately 02:00 UT on May 12, 2012. The event was clearly visible from both STEREO viewpoints, and the CME apex was observed at progressively larger elongation angles in STEREO-B imagery compared to STEREO-A (note the position of the apex in Figure 5 and in Movie S3). This suggests that the CME was closer to quadrature-view from the STEREO-B perspective, consistently with the coronagraph analysis reported in Section 3.1.2 (see Figure 1a for the position of the STEREO spacecraft).

In order to follow the propagation of the CME under study through both HI cameras, we use time–elongation maps (e.g., Davies et al., 2009; Sheeley et al., 2008) produced from running-difference images. Within these time–elongation maps, a propagating structure such as a CME appears as a bright front followed by a dark front. This is due to the increase and subsequent decrease in density and allows features to be tracked in elongation as a function of time. This is performed on the CME under investigation here, which we track for over 2.5 days in HI-A to an elongation of ∼30° and for over 1.5 days in HI-B to an elongation of ∼35°. The resulting time–elongation maps, with the corresponding CME tracks, are shown in Figures 5c and 5d.

Furthermore, the CME under study is listed in the HELiospheric Cataloging, Analysis and Techniques Service (HELCATS) catalogs. The HELCATS project ran from 2014 to 2017 and aimed, among other goals, to catalog and analyze solar transients (such as CMEs) detected in the STEREO/SECCHI/HI cameras. This event

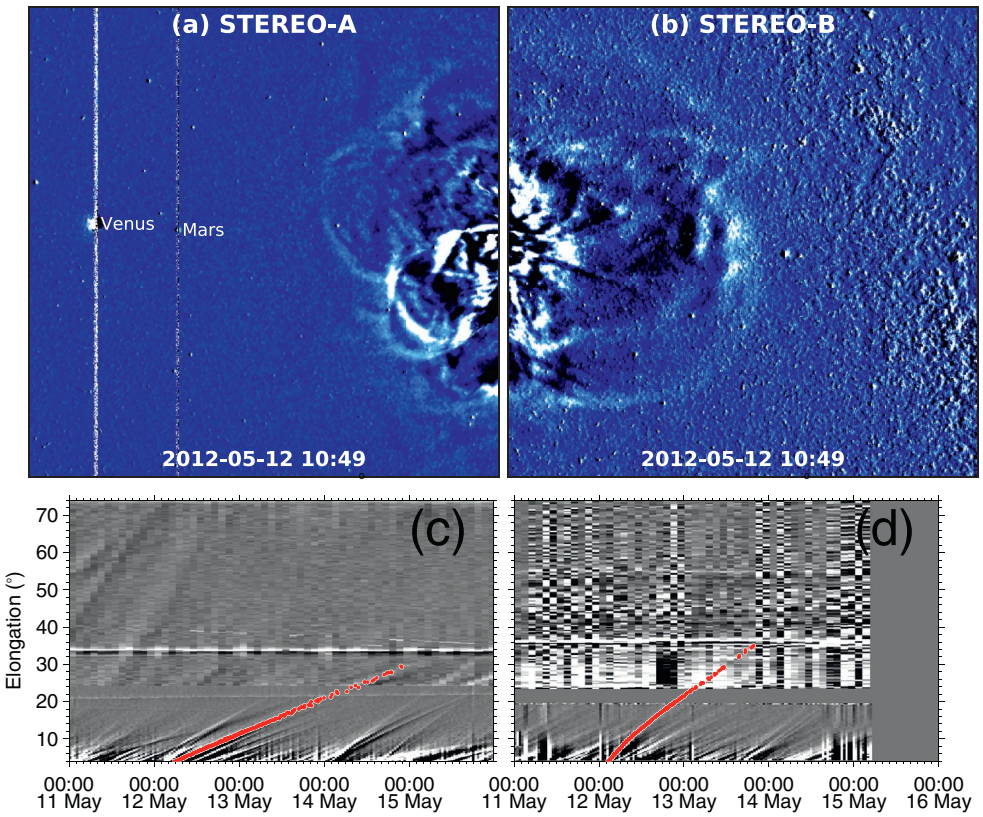

Figure 5. The May 11, 2012 CME as seen in images from the STEREO/SECCHI/HI cameras. (a and b) Snapshots of the CME in running-difference images taken with the (a) HI1-A and (b) HI1-B cameras. The projected locations of Venus and Mars are marked in panel (a). (c and d) Time–elongation maps from (c) STEREO-A and (d) STEREO-B. The CME tracks are marked in red. The maps are constructed along position angles of 90° for STEREO-A and 264° for STEREO-B, that is, close to the ecliptic plane (the position angle of Earth was ∼89.9° from the STEREO-A perspective and ∼264.4° from the STEREO-B perspective). CME, coronal mass ejection; SECCHI, Sun Earth Connection Coronal and Heliospheric Investigation; STEREO, Solar Terrestrial Relations Observatory.

is included in the HICAT catalog (Harrison et al., 2018), which was generated through visual inspection of background-subtracted and difference HI1 images, and in the HIGeoCAT catalog (Barnes et al., 2019), which was generated using time–elongation maps and applying single-spacecraft fitting techniques to derive CME kinematic properties. In both catalogs, the CME is labeled as HCME_A__20120511_01 for STEREO-A and HCME_B__20120512_01 for STEREO-B. We remark that, in both HICAT and HIGeoCAT, CMEs are identified using single-spacecraft data, hence the STEREO-A and STEREO-B observations are reported separately. Of the fitting techniques used in HIGeoCAT, we report here the results obtained with the Self-Similar Expansion (SSE; Davies et al., 2012; Möstl & Davies, 2013) fitting technique with a fixed half-width of 30° (hereafter, SSEF30) applied to time–elongation single-spacecraft data. In the SSE model, CMEs are assumed to have a circular front and to propagate radially with a constant speed and half-width. We note that the SSEF30 results obtained using STEREO-B data are consistent with the GCS results reported in Section 3.1.2, that is, the CME propagates in direction $(\theta, \phi) = (-9°, -19°)$ and with a speed of 869 kms^{-1}. SSEF30 results based on STEREO-A data, however, are significantly different, reporting a propagation direction of $(\theta, \phi) = (-4°, -54°)$ and a speed of 2008 kms^{-1}. Since, as stated above, the May 11, 2012 CME was closer to quadrature view (i.e., with less projection effects) from STEREO-B than from STEREO-A, we expect the fitting results retrieved from STEREO-B data to be more accurate.

3.2. The May 17, 2012 Eruption

The second eruptive event that we focus on in this work initiated from AR 11476 on May 17, 2012 around 01:00 UT. Since in this case we are mostly interested in the release of energetic particles, rather than the

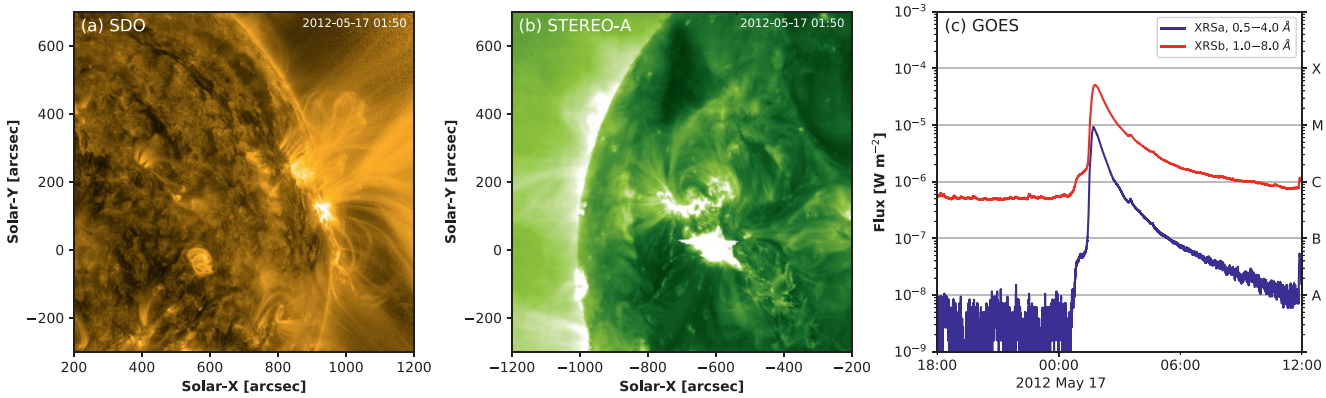

Figure 6. Overview of the May 17, 2012 eruption. (a) SDO/AIA image of the source region (AR 11476) in the 171 Å channel shortly after the flare onset time. (b) STEREO/SECCHI/EUVI-A image of the source region in the 195 Å channel taken at the same time as (a). (c) GOES-15/XRS soft X-ray flux, showing the occurrence of an M5.1 flare. AIA, Atmospheric Imaging Assembly; EUVI, Extreme UltraViolet Imager; GOES, Geostationary Operational Environmental Satellites; SDO, Solar Dynamics Observatory; SECCHI, Sun Earth Connection Coronal and Heliospheric Investigation; STEREO, Solar Terrestrial Relations Observatory; XRS, X-ray Sensor.

CME eruption and evolution itself, we provide here a brief overview of the event. The source region was located close to the western limb from Earth's perspective (N11W76) and on disc (on the north-eastern quadrant) from STEREO-A's perspective, while it was fully back-sided from STEREO-B's viewpoint (see Figure 1b). The large-scale CME associated with this eruption was fast, with a speed above 1,500 kms^{-1}, and large, as it appeared as a halo from all three viewpoints. An intense "snowstorm," caused by high-energy protons striking the cameras, was seen in both SOHO/LASCO coronagraphs (C2 and C3) starting around 02:00 UT. Furthermore, the GOES/XRS instrument reported an M5.1 flare associated with this event, starting at 01:25 UT, peaking at 01:47 UT, and ending at 02:14 UT. Figure 6 provides images of the CME's source region as seen by SDO (Figure 6a) and STEREO-A (Figure 6b), together with the soft X-ray flux measured by GOES-15 (Figure 6c).

The May 17, 2012 eruption has been studied, for example, by Gopalswamy et al. (2013), Li et al. (2013), Shen et al. (2013), and Rouillard et al. (2016), hence the reader is referred to these articles for additional information and images on the eruptive event and the CME's propagation through the solar corona. In particular, we note that Gopalswamy et al. (2013) estimated the shock formation and SEP release heights for the May 17 CME to be 1.38 $R_\odot$ (at 01:32 UT) and 2.32 $R_\odot$ (at 01:40 UT) from the solar center, respectively. Together with the occurrence of the M5.1 flare, this suggests that the May 17, 2012 SEP event had contributions from both flare-accelerated and shock-accelerated particles, which is what Cane et al. (2010) concluded to be the most likely scenario for large SEP events. This conclusion was, in fact, reached by Li et al. (2013), who estimated that electrons were accelerated by the flare at 01:29 UT and protons were accelerated by the CME-driven shock at 01:39 UT from an altitude of 3.07 $R_\odot$. Furthermore, Shen et al. (2013) suggested that the May 17, 2012 CME was composed of two nearly simultaneous ejecta that erupted from the same active region and neutral line, leading to a CME–CME shock interaction scenario. Finally, previous studies reported also the presence of a so-called EUV wave (e.g., B. J. Thompson et al., 1998; Zhukov & Auchère, 2004), visible from both SDO's and STEREO-A's viewpoints.

4. CME Propagation Modeling

In this section, we propagate the May 11, 2012 CME using different techniques and evaluate its impact at different planets and spacecraft scattered throughout the inner heliosphere. The results of the propagation models that we consider in this work are summarized in Table 1.

4.1. (S)SSE Propagation

We first evaluate the impact of the May 11, 2012 CME at various locations in interplanetary space using HI data (see Section 3.1.3). Considering again the HELCATS products, we initially search for the CME

Table 1
CME Arrival Times From the Different modeling Techniques Presented in Section 4

Model	Venus	Earth	Spitzer	MSL	Mars
SSEF30–A	—	—	05/12 20:18	05/13 07:55	05/13 11:51
SSEF30–B	05/13 09:11	05/14 04:40	—	05/15 03:18	05/15 13:52
SSSE	05/14 19:15	05/17 18:51	05/15 15:01	05/17 00:13	05/17 14:57
DBM	05/14 00:08	05/15 00:20	05/14 23:42	05/16 14:42	05/17 05:49
Enlil (S)	05/13 19:33	05/14 21:30	05/14 20:03	05/16 05:54	05/16 21:58
Enlil (E)	05/14 01:00	05/15 17:52	05/15 21:07	05/17 03:06	05/17 23:27

Note. Dates are shown in the format MM/DD HH:MM. The notations "(S)" and "(E)" denote shock and ejecta, respectively.

under study in the ARRCAT catalog (Möstl et al., 2017), which was generated from the list of events in HIGeoCAT by predicting their impact throughout the heliosphere. The predictions were made using the SSEF30 model introduced in Section 3.1.3. We note that, in ARRCAT, HCME_A__20120511_01 is reported to arrive at MSL and Mars, while HCME_B__20120512_01 is predicted to impact Venus and Earth as well. The exact arrival times predicted by ARRCAT (SSEF30-A and SSEF30-B) are reported in Table 1. We emphasize that Spitzer is not included as a possible target in ARRCAT. Nevertheless, we evaluate arrival estimates at the spacecraft using the CME parameters listed in HIGeoCAT and the equations reported in Möstl and Davies (2013). This results in an impact according to SSEF30-A and a close miss according to SSEF30-B.

Since the CME under study was well-visible in both STEREO spacecraft, we also use the two-spacecraft version of the SSE model, that is the Stereoscopic Self-Similar Expansion (SSSE; Davies et al., 2013) model, to triangulate the CME position over the ∼1.5 days in which the event was observed by both spacecraft using time–elongation data. This model also assumes that the CME possesses a circular cross-section in the plane in which the CME is observed (in our case, this is the ecliptic) and a constant half-width. To estimate the half-width to use in this case, we use the formulas in Rodriguez et al. (2011) to calculate the maximum angular extent of a CME in both latitude and longitude using the GCS parameters as input. This results in an half-angular extent of 58° in latitude and 54° in longitude. Since the SSSE is a 2D model, we are only interested in the longitudinal extent of the CME, hence we set a half-width of 54°. In order to extrapolate the position of the CME beyond the time it was last observed, we fit a second-order polynomial to the distance of the CME apex as a function of time. We also assume that the CME continues to propagate in a constant direction beyond its last observed value. As a result of this extrapolation we expect the CME front to pass over Venus, Earth, Spitzer, MSL, and Mars. Table 1 reports the arrival times at all the impacted locations, and Figure S2 shows the position of the tracked CME front together with the resulting CME arrival times and speeds at the three planets (Venus, Earth, and Mars).

4.2. DBM Propagation

As a further indication of the CME propagation and impact at different planets and spacecraft, we the drag-based model (DBM; Vršnak et al., 2013), which computes analytically the propagation of CMEs using aerodynamic drag equations and with the assumption of a constant background speed and constant drag parameter. For our run, we use an ambient solar wind speed of 450 kms^{-1} (from measurements of the solar wind speed at the spacecraft in the inner heliosphere a few days after the eruption time) and a drag parameter of 1×10^{-7} km^{-1} (i.e., the mean value found by Vršnak et al., 2013). In the simplest version of the DBM, the geometry of CMEs is that of a 2D circular arc centered at the Sun and moving outwards. The CME parameters that we introduce in the tool are entirely derived from the GCS reconstructions presented in Section 3.1.2: height of 14.4 $R_{\odot}$ on May 12, 2012 at 01:54 UT, speed of 1,005 kms^{-1} (which is the speed between the reconstructions at 01:24 and 01:54 UT, when the CME reached the height of 14.4 $R_{\odot}$), half-width of 54° (again, the full longitudinal extent of the CME using the formulas by Rodriguez et al., 2011), and

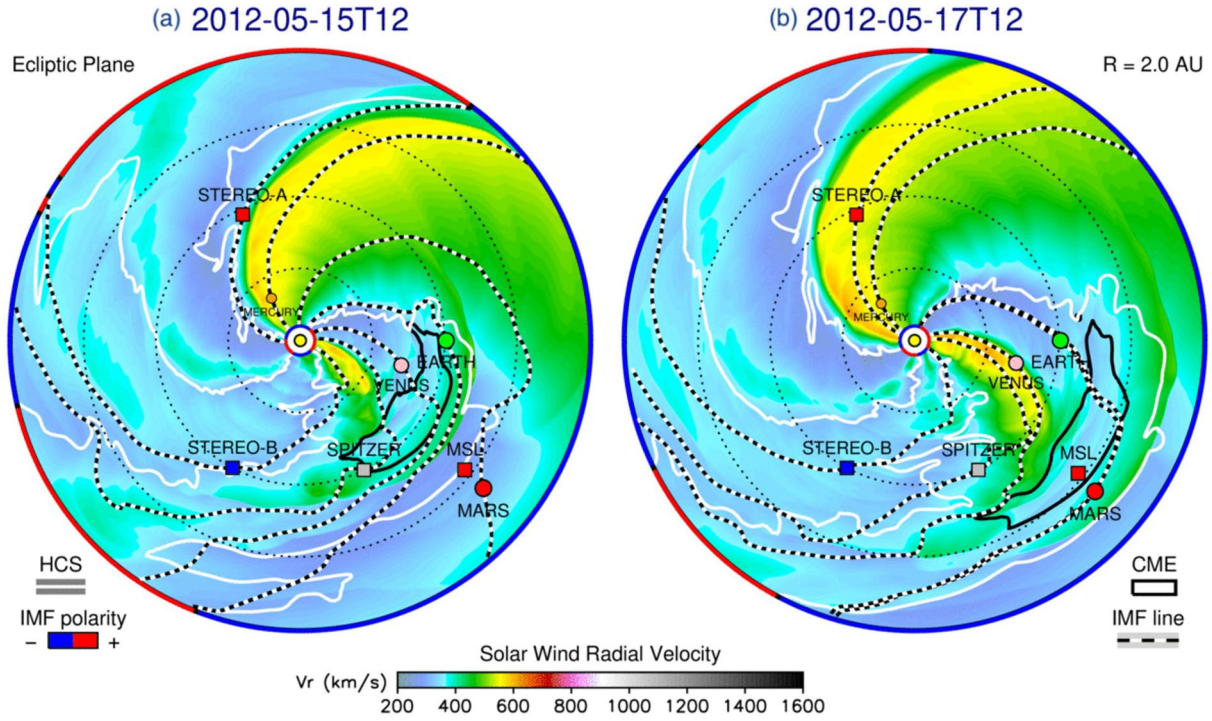

Figure 7. Screenshots from the WSA–Enlil+Cone simulation. The parameter shown in the plots is the solar wind radial speed in the ecliptic plane on (a) May 15, 2012 12:00 UT, and (b) May 17, 2012 12:00 UT.

longitude of −30° (in Stonyhurst coordinates). With the initial set of parameters described above, impacts are estimated at Venus, Earth, Spitzer, MSL, and Mars. The resulting arrival times at the different planets and spacecraft are reported in Table 1, and a visual representation of the CME propagated with the DBM is shown in Figure S3.

4.3. Enlil Simulation

The final CME propagation model that we employ in this study is the 3D heliospheric magnetohydrodynamic (MHD) Enlil (Odstrcil, 2003; Odstrcil et al., 2004) model. Enlil uses the Wang–Sheeley–Arge (WSA; Arge et al., 2004) coronal model to simulate the background solar wind from its inner boundary (located at 21.5 $R_\odot$ or 0.1 AU) onwards. In this case, we set the outer boundary of the simulation domain at 2 AU, that is, including the whole inner heliosphere. CMEs can be modeled through insertion at the inner boundary of the heliospheric domain. In this work, we employ the WSA–Enlil+Cone model, in which CMEs are injected as spherical hydrodynamic structures that lack an internal magnetic field (i.e., there is no internal flux rope structure). Again, we derive the CME initial parameters from GCS reconstructions (see Section 3.1.2). We obtain the injection time at the inner boundary by propagating the CME from its last GCS reconstruction (on May 12, 2012 at 01:54 UT) up to 21.5 $R_\odot$ using a constant speed derived from this last GCS reconstruction and a reconstruction made from data obtained 30 min earlier (in this case, at 01:24 UT). This yields an injection time of May 12, 2012 at 03:16 UT with a speed of 1,005 kms^{-1}. The CME cone that we model has an elliptical cross-section, and we derive its dimensions by "cutting" an elliptical cross-section out of the GCS shell (based on Thernisien, 2011). The resulting values for the half-angular extent of the major and minor radii are 46.75° and 37.89°, respectively. Finally, the values for latitude (−10°), longitude (−30°), and tilt angle (−65°) are taken directly from GCS results. The resulting arrival times at different locations throughout the heliosphere are reported in Table 1, and two screenshots from the simulation results are shown in Figure 7. The two separate rows for Enlil reported in Table 1 refer to the shock (S) and ejecta (E) arrival times. As was the case for the previous models, we expect the CME to impact Venus, Earth, Spitzer, MSL, and Mars.

5. In-situ Measurements

Next, we analyze in-situ data from multiple locations scattered throughout the inner heliosphere to evaluate the predicted impacts presented in Section 4. Namely, we search for interplanetary signatures of the May 11, 2012 CME at Venus (0.7 AU), Earth (1.0 AU), Spitzer (1.0 AU), MSL (1.4 AU), and Mars (1.6 AU). At each location, in addition to looking for ICME signatures from the May 11, 2012 CME, we search for SEP signatures from the May 17, 2012 event.

5.1. Measurements at Venus

The first (in terms of distance from the Sun, see Figure 1) location for which an impact of the May 11, 2012 CME is predicted is Venus. Indeed, observations around Venus made by the VEX spacecraft following the eruption reveal a period of transient disturbances. Such measurements are reported in Figure 8. In particular, an interplanetary shock was detected by VEX on May 13, 2012 at 17:10 UT. After a long-duration sheath region, flux rope-like signatures could be identified from May 14, 2012 at 19:23 UT through May 16, 2012 at 01:30 UT. We utilize here the terminology "flux rope-like" rather than the more common "magnetic cloud" because the boundaries were determined from magnetic field data only, since plasma data are not provided by VEX continuously (as explained in Section 2, the ASPERA-4 instrument was operational at periapsis and apoaxis only, i.e., about twice per Earth day). The long duration of the sheath region between the interplanetary shock and the following ejecta is likely the result of the interaction of the May 11 CME with a small preceding interplanetary structure. Solar observations from STEREO prior to the eruption of the May 11 CME reveal the presence of several minor eruptions characterized by a jet-like morphology in coronagraph images (see Vourlidas et al., 2013, 2017, for a classification of CME morphology types) that were possibly Earth-directed. Observations following the eruption of the May 11 CME did not feature CME events large enough to cause the interplanetary signatures shown in Figure 8, indicating that the Sun–Venus connection of the CME is likely correct.

A possible interpretation for the features observed before the flux rope-like ejecta is that the interplanetary shock driven by the May 11, 2012 CME (solid vertical line in Figure 8) propagated through the preceding structure, while the following sheath material remained behind. Previous studies have shown that a faster shock can indeed travel through a slower, preceding structure (e.g., Kilpua, Good, et al., 2019; Lugaz et al., 2013). A possible "interface" between the preceding interplanetary structure and the following sheath region driven by the May 11, 2012 CME is indicated by a dashed vertical line in Figure 8 (estimated via the rapid change in direction in the magnetic field Z-component). The speed profile within the flux rope-like structure (shaded region in Figure 8) appears nearly flat, suggesting that the ejecta was not expanding as it passed Venus. We emphasize, however, that only two velocity data points fall within the flux rope-like structure and, thus, these conclusions may not be representative of the fine structure of the speed profile. Visual inspection of the ejecta magnetic field shows a rotation of the Y-component from west to east and a rotation of the Z-component from south to north. This suggests that the corresponding flux rope is right-handed and at an intermediate orientation between a south–west–north (SWN) and a west–north–east (WNE) type. We also estimate the orientation of the flux rope using two techniques. The first is the minimum variance analysis (MVA; Sonnerup & Cahill, 1967), where the flux rope axis corresponds to the MVA intermediate variance direction. The orientation of the flux rope axis resulting from MVA is $(\Theta, \Phi) = (50°, 261°)$, thus in the intermediate state between a SWN- and a WNE-type flux rope, consistently with what is suggested by visual inspection of the magnetic field data. We also fit the flux rope using the analytical Circular-Cylindrical (CC) model described in Nieves-Chinchilla et al. (2016). According to the CC model, the flux rope is right-handed, its axis has orientation $(\Theta, \Phi) = (24°, 256°)$, and the impact parameter is $y0/R = -0.22$, with $R = 0.15$ AU being the radius of the cloud. The two methods yield an almost identical Φ angle for the flux rope axis, while the Θ angle differs by ~25°. Nevertheless, given the usual uncertainties related to all fitting techniques (e.g., Démoulin et al., 2018; Lepping et al., 2003; Riley et al., 2004), these results can be deemed mostly consistent, thus indicating a right-handed flux rope with a low-to-intermediate inclination.

Finally, we note a remarkable increase in the background counts measured by VEX/IMA (Figure 8k) during the early hours of May 17, 2012 indicating that an SEP event had impacted Venus. The enhancement of background levels in the ASPERA suite, in fact, corresponds to sufficiently energetic particles that are able

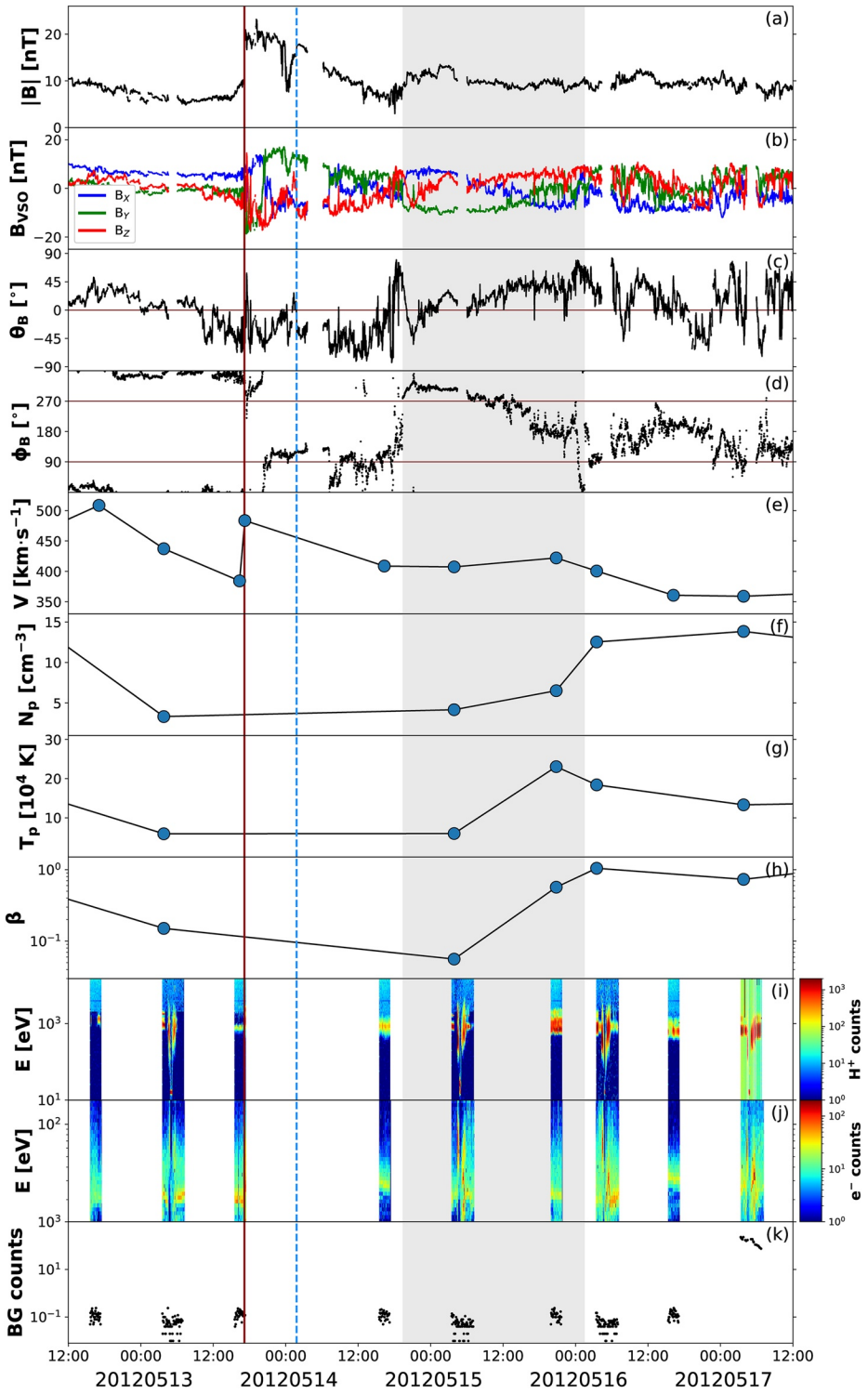

Figure 8. Measurements at Venus around the expected arrival time of the May 11, 2012 CME, revealing the passage of an interplanetary disturbance. All data are taken from VEX. The solid vertical line indicates the arrival of the interplanetary shock, while the dashed vertical line marks a possible interface between the preceding material and the following sheath driven by the May 11, 2012 CME. The shaded area corresponds to the estimated flux rope-like interval. The periods in which VEX is within Venus' bow shock have been removed from the magnetic field data set. The parameters shown are: (a) magnetic field magnitude, (b) magnetic field components in Venus Solar Orbital (VSO) Cartesian coordinates, (c) θ and (d) ϕ angles of the magnetic field in VSO angular coordinates, (e) solar wind speed, (f) proton number density, (g) proton temperature, (h) plasma β, (i) proton and (j) electron energy distribution, and (k) background counts. CME, coronal mass ejection; VEX, Venus Express.

to penetrate the instrument (e.g., Futaana et al., 2008; Ramstad et al., 2018). Since ASPERA-4 was operational close to periapsis and apoapsis only, the background count enhancement was first observed at 03:22 UT after a data gap, thus it is not possible to establish the "true" onset time and peak intensity of the SEP event at Venus. According to the May 17 eruption overview presented in Section 3.2 and taking into account a particle propagation time of ∼10–15 min, we would expect various locations in the inner heliosphere to see an SEP event some time before 02:00 UT on May 17, 2012. This is consistent with the "descending" profile seen in the IMA background counts, suggesting an earlier onset and peak. Thus, the background enhancement seen at VEX seems to be indeed due to the May 17 eruption. Furthermore, we note that the SEP event at Venus is not observed inside the May 11, 2012 ICME ejecta, but ∼1 day after the passage of what we defined as the trailing edge of the flux rope-like structure. However, considering the CME propagation direction estimated in Sections 3.1 and 4, it is likely that Venus was immersed in the CME leg, CME wake, or some other trailing structure in the IMF at the time of the SEP event.

5.2. Measurements at Earth

The next location for which we evaluate a possible impact of the May 11, 2012 CME and May 17, 2012 SEP event is Earth. Given the relatively small separation between Venus and Earth (∼0.3 AU in radial distance and ∼15° in longitude, see Figure 1), we expect to observe relatively similar ICME signatures that, with the aid of continuous plasma measurements, could strengthen the interpretation reported in Section 5.1. Indeed, similarly to observations around Venus, measurements of the solar wind taken from Earth's Lagrange L1 point during the days following the May 11, 2012 eruption reveal clear signatures of a transient period of disturbed IMF and plasma flow. Figure 9 shows magnetic field and plasma data taken by Wind together with GOES proton flux and neutron monitor data from the SOPO station. Such measurements show that an interplanetary shock impacted the spacecraft on May 15, 2012 at 01:25 UT, followed by a long-duration sheath. Clear magnetic cloud signatures were visible from May 16, 2012 at 15:57 UT through May 17, 2012 at 22:20 UT.

The sequence of features within the ICME generally matches the measurements at Venus (Section 5.1), the interplanetary shock (solid vertical line in Figure 9) being followed by material that appears to belong to two interacting structures. Again, we have marked in Figure 9 (with a dashed vertical line) the possible "interface" separating the two. Interestingly, the first portion shows significant expansion from Venus to Earth (from 8.6 to 19.3 h), while the following portion of sheath features only minimal expansion (from 17.6 to 19.2 h). This can be explained considering the ambient solar wind ahead of the ICME: at Venus (Figure 8e), the interplanetary shock is preceded by the trailing portion of a fast stream and the following slow wind, while at Earth (Figure 9e), the shock has traveled through the slow stream and has caught up with the fast one. This has likely facilitated the expansion of the small structure immediately following the shock, while the remaining portion of material (which we associated to the sheath region of the May 11, 2012 CME) shows signatures of compression (with an increasing speed profile and enhanced density) rather than expansion.

The magnetic cloud-type ICME ejecta (shaded region in Figure 9) is reported in both the Richardson & Cane ICME list (hereafter R&C list; Cane & Richardson, 2003; Richardson & Cane, 2010) and the NASA-Wind ICME list (hereafter N-C list; Nieves-Chinchilla et al., 2018, 2019). The R&C list reports the ejecta measured at Earth as a clear magnetic cloud, featuring bidirectional electrons and lacking signatures of expansion. We also note that, in the R&C list, the May 11, 2012 CME that we analyzed through remote-sensing imaging in Section 3 is reported as the most probable solar counterpart of this event. The N-C list reports the ejecta as a flux rope, with an apparent expansion velocity of -7 kms^{-1} and a distortion parameter of 0.57 (the distortion parameter is defined as the fraction of the magnetic obstacle where 50% of the total magnetic field magnitude is accumulated). Again, these signatures show no expansion of the ejecta, but rather its slight compression at the back, which is consistent with the presence of faster wind following it. Indeed, the magnetic cloud hardly features any expansion even when considering its evolution from Venus to Earth (its duration goes from 30.1 h at Venus to 30.4 h at Earth). Figure 9i shows the electron pitch-angle-distribution (PAD) parameter (EPP) for five energy levels. The EPP was defined by Nieves-Chinchilla et al. (2016) and consists of the average electron intensities close to 0° and 180° normalized to those close to 90°, thus quantifying the bidirectionality of electrons within a magnetic obstacle from PAD data. The profiles show

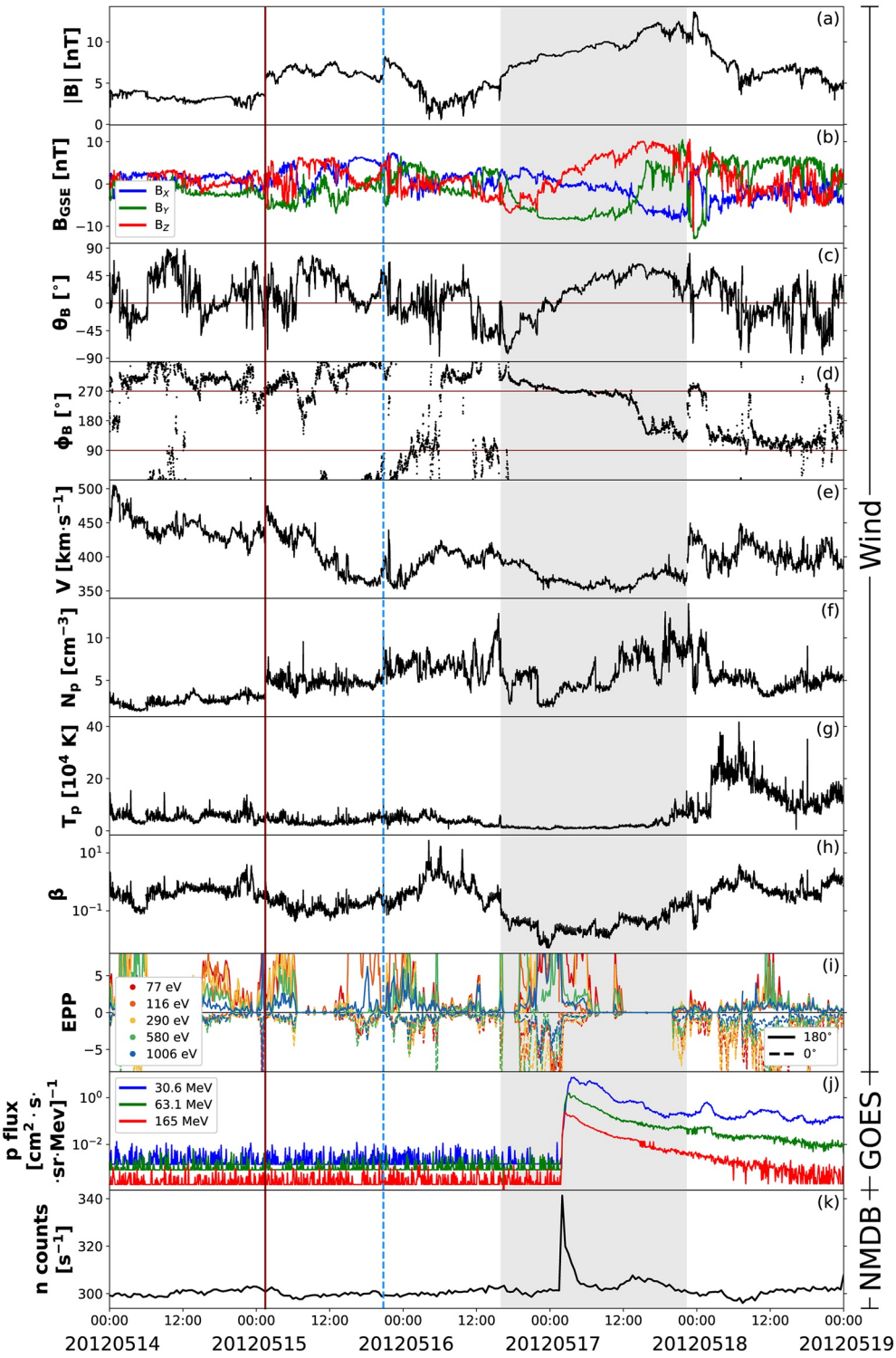

Figure 9. Measurements at Earth around the expected arrival time of the May 11, 2012 CME, revealing the passage of an interplanetary disturbance. Data are taken from (a–i) Wind, (j) GOES-13, and (k) the SOPO neutron monitor. The solid vertical line indicates the arrival of the interplanetary shock, while the dashed vertical line marks a possible interface between the preceding material and the following sheath driven by the May 11, 2012 CME. The shaded area corresponds to the estimated magnetic cloud interval. The parameters shown are: (a) magnetic field magnitude, (b) magnetic field components in Geocentric Solar Ecliptic (GSE) Cartesian coordinates, (c) θ and (d) ϕ angles of the magnetic field in GSE angular coordinates, (e) solar wind speed, (f) proton number density, (g) proton temperature, (h) plasma β, (i) electron pitch angle distribution parameter for five energy levels, (j) energetic proton flux, and (k) neutron monitor counts per second. CME, coronal mass ejection; GOES, Geostationary Operational Environmental Satellites; SOPO = South Pole.

signatures of bidirectionality during the first half of the flux rope and a drop to near zero for the second half. This suggests that the magnetic field lines at the front are still connected to the Sun, while in the rear part at least one leg appears to be disconnected (PAD spectra exhibit signatures of one-directional strahl, data not shown). Regarding the magnetic structure of the magnetic cloud, visual inspection of the magnetic field shows a rotation of the *Y*-component from west to east and a rotation of the *Z*-component from south to north. The orientation of the flux rope axis from MVA is (Θ, Φ) = (46°, 271°), which is almost identical to the orientation found at Venus using the same method. The N-C list also provides fitting results for the flux rope using the CC model, according to which the flux rope is right-handed, its axis has orientation (Θ, Φ) = (29°, 229°), and the impact parameter is $y0/R = -0.38$, with $R = 0.13$ AU being the radius of the cloud. In addition to the uncertainties related to flux rope fitting techniques mentioned in Section 5.1, in this case the difference in axis orientation from the MVA and CC methods may also depend on the fact that the flux rope boundaries do not coincide exactly (in the N-C list, the trailing edge is marked about 4 h later than the one considered in this work). The importance of the boundary selection to increase the level of agreement across different models was quantified by Al-Haddad et al. (2013). Nevertheless, both results are consistent with a right-handed flux rope with a low-to-intermediate inclination (i.e., somewhere between a SWN- and a WNE-type), in agreement with measurements at Venus (Section 5.1).

Finally, Figures 9j and 9k shows proton flux and neutron monitor data. A Forbush decrease (Forbush, 1937; Hess & Demmelmair, 1937) can be seen in the SOPO time series starting around 02:30 UT on May 15, 2012 that is, shortly after the interplanetary shock arrival at Wind. We remark that neutron monitor data are collected from ground-based stations, while Wind is located at Earth's L1 point, thus the slight (∼1-h) delay indicates that the features clearly correspond to the same event. This Forbush decrease was also analyzed by Freiherr von Forstner et al. (2019), who connected 45 ICMEs from the Sun to the MSL spacecraft using STEREO/HI data (accordingly, more information regarding the findings of this study can be found in Section 5.4). The most striking feature in the neutron monitor time series, however, is the considerable peak in the count rate starting at 01:56 UT on May 17, 2012 that is, during the passage of the magnetic cloud at Earth, indicating the occurrence of a ground-level enhancement (GLE; e.g., Nitta et al., 2012). This corresponds to the SEP event registered by GOES in proton flux measurements, with onset between 01:55 and 02:00 UT. The May 17, 2012 SEP event at Earth was studied in detail in the literature (e.g., Battarbee et al., 2018; Ding et al., 2016; Gopalswamy et al., 2013; Li et al., 2013; Plainaki et al., 2014; Rouillard et al., 2016), being associated with the first GLE of solar cycle 24 (GLE71), and was even detected at the International Space Station (Berrilli et al., 2014). Rouillard et al. (2016) suggested that the passage of the magnetic cloud facilitated magnetic connectivity between the May 17 eruption source region and Earth.

5.3. Measurements at the Spitzer Space Telescope

Also at ∼1 AU but separated by ∼70° from Earth (see Figure 1) was Spitzer. Although this telescope was dedicated to infrared measurements of deep space, it has been shown that it can be used to investigate space weather events (Cheng et al., 2014). Specifically, energetic particles of both solar and extra-solar origin can impact multiple subsystems on the spacecraft, hence Spitzer can act as a space weather monitor for SEP events of sufficiently high energies (≥100 MeV). In this study, we focus on the high-energy particle hits on Spitzer's main science instrument, IRAC, which result in saturated pixels in the infrared images taken by the camera. Such affected pixels are flagged as "radhits" and masked, in order to ensure that they are excluded from composite images of the observations. On average, IRAC measures about 4–6 radhits per second (depending on the phase of the solar cycle) due to galactic cosmic rays (Lowrance et al., 2018). During May 2012, this "baseline number" was estimated to be 4 ± 0.8 radhits per second. Thus, a number of detected radhits higher than 4 may correspond to a space weather event of solar origin.

The radhits measured by IRAC during May 10–20, 2012 are shown in Figure 10. As expected, most of the data points are clustered around the value of 4. The propagation models that we used in this work (see Section 4 and Table 1) estimated a CME impact at Spitzer to take place around May 14–15, 2012. We do not observe an increase in radhits during that period, suggesting that, if the May 11 CME did indeed impact Spitzer, it was not associated with high-energy particles (as it was the case in the study performed by Amerstorfer et al., 2018, on a CME that erupted on November 3, 2010). This is not surprising, since the ICME appeared rather slow at both Venus (Section 5.1) and Earth (Section 5.2). Nevertheless, we do observe an increase in

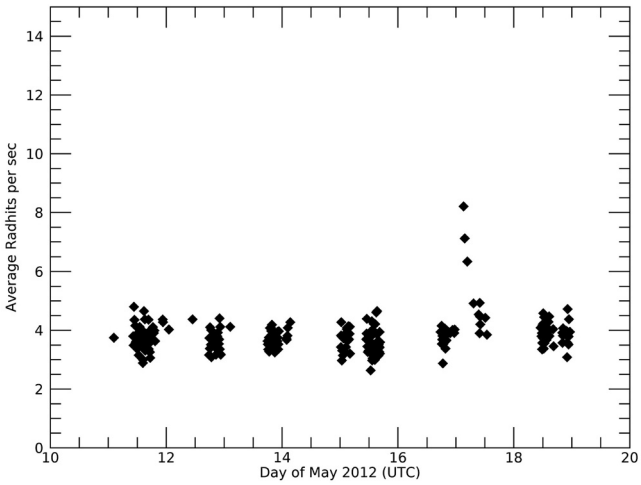

Figure 10. Radhits per second measured by the IRAC instrument onboard Spitzer during the days following the May 11, 2012 CME eruption. The gaps correspond to times in which IRAC was not taking data due to downlinking. Each data point corresponds to exposure times of 12, 30, or 100 s, and is averaged over a number of frames in the range 5–25. The overall data set has an average of 3.77 ± 0.61 radhits per second. CME, coronal mass ejection; IRAC, Infrared Array Camera.

counts starting on May 17, 2012 at 03:10 UT, with the measured radhits reaching a value > 8. As it was the case for particle measurements at Venus (Section 5.1), the increase follows a several-hour data gap, hence it is not possible to establish an exact onset time for the event. Nevertheless, the timing and descending profile of the increase strongly hint toward an earlier onset and a "true peak value" higher than 8.2 radhits per second, consistent with the SEP event being associated with the May 17 eruption. Since Spitzer was separated by ~150° in longitude from the flaring site, it follows that there is no possibility for the two heliolongitudes to be magnetically connected under nominal Parker spiral conditions. Hence, it is likely that the magnetic connectivity required for the observed impulsive feature of the SEPs was provided by the May 11 CME, which was being crossed by Spitzer at the time of the flare.

5.4. Measurements at the Mars Science Laboratory

At the time of the CME under study, the MSL spacecraft was approaching the end of its cruise phase, before safely landing the Curiosity rover on Mars on August 6, 2012. It was at a heliocentric distance of ~1.4 AU and its longitude was ~35° east of Earth (see Figure 1). Even though the RAD instrument was designed to measure the particle radiation environment on the surface of Mars, it was active during most of the cruise phase and collected data of the interplanetary radiation environment for future crewed missions to Mars (Zeitlin et al., 2013), detecting several Forbush decreases and SEP events (Guo et al., 2015).

Radiation dose measurements taken by MSL/RAD during the days following the May 11, 2012 eruption are shown in Figure 11. Again, we find in the data clear signatures of the SEP event related to the May 17, 2012 eruption (also reported by Battarbee et al., 2018), starting at 02:04 UT and suggesting that the May 11 CME was also being crossed by MSL at that time. Therefore, we search for a possible Forbush decrease onset before the arrival of the SEPs. We tentatively identify such onset to take place on May 15, 2012 at 13:30 UT (marked with a solid vertical line in Figure 11). Unfortunately, the SEP event of May 17 does not allow us to follow the full development of the Forbush decrease, hence it is not possible to declare with certainty whether the decrease is a "classical" two-step one. A Forbush decrease that develops in two steps usually

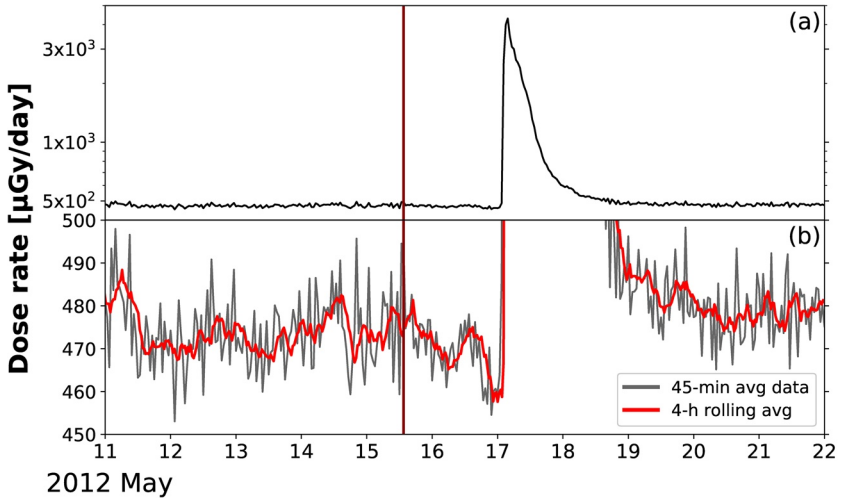

Figure 11. Radiation dose measurements taken by MSL/RAD en route to Mars. Panel (b) is a zoomed-in version of the *y*-axis of panel (a). The time of the Forbush decrease onset (used to estimate the shock arrival time) is indicated with the solid vertical line. MSL, Mars Science Laboratory; RAD, Radiation Assessment Detector.

indicates the arrival of an interplanetary shock, corresponding to the first step, and its following ICME ejecta, corresponding to the second step (Cane, 2000). Nevertheless, the Forbush decrease onset time that we identified is consistent with the analysis performed by Freiherr von Forstner et al. (2019), who reported an arrival time at MSL on May 15, 12:00 UT (event 20120512_01 in their study). The authors connected this Forbush decrease with the one measured at Earth earlier on the same day (see Section 5.2) and with the CME observed in HI1-B imagery (see Section 3.1.3), in agreement with our analysis of the same event.

5.5. Measurements at Mars

At 1.6 AU from the Sun and almost perfectly aligned with MSL (<1° separation in longitude, see Figure 1) was Mars. There were no spacecraft equipped with a magnetometer in orbit around Mars at the time of this study, hence it is not possible to analyze the magnetic structure of the May 11, 2012 CME. Nevertheless, we take advantage of the extensive data sets that are available from two spacecraft to estimate the arrival time of the interplanetary shock and the boundaries of the following ICME ejecta. In particular, we complement the solar wind and particle data collected by MEX/ASPERA-3 and MOdy/HEND with measurements performed inside the Martian induced magnetosphere by MEX/MARSIS. Since Mars is not protected by an intrinsic magnetic field, the increased dynamic pressure accompanying periods of disturbed solar wind conditions is able to push the plasma boundaries of the system (e.g., bow shock, magnetic pileup boundary, ionopause) to lower altitudes quite efficiently (e.g., Lee et al., 2017; Luhmann et al., 2017; Morgan et al., 2014; Sánchez-Cano et al., 2017, 2020). Hence, the level of compression of the Martian induced magnetosphere can help to determine whether a solar transient has impacted the planet. In this study, we focus on the altitude of the outbound magnetic pileup boundary crossings for successive orbits. Since the MEX orbit precession is minimal during the period that we investigate (11 days), we can assume that the boundary crossings should always occur at similar altitudes in the case of a static system.

Figure 12 shows plasma and energetic particle measurements taken by MEX and MOdy following the eruption of the CME under study. Several signatures in these data indicate that an interplanetary shock (solid vertical line in Figure 12) impacted Mars on May 16, 2012 around 06:00 UT. Namely, we observe significant compression of the Martian magnetic pileup boundary between two successive orbits (Figure 12a, showing that the altitude of the crossings lowered from ∼750 to ∼400 km), a steep increase in the speed profile (Figure 12b), enhancement in electron counts (Figure 12f), and the onset of a Forbush decrease (Figure 12i). However, as it was the case for MSL (Section 5.4), the SEP event of May 17 is seen at Mars as well, preventing us from following the whole development of the Forbush decrease and, therefore, possibly estimating the ejecta leading edge time. Nevertheless, the presence of SEP signatures, seen in both MEX/IMA background counts (Figure 12g) and MOdy/HEND count rates (Figure 12h) and starting at 02:16 UT, suggests that the ICME ejecta was also being crossed by Mars at the time of the May 17 eruption. If we consider the period of depressed proton temperature following the shock arrival (one of the "classic" in-situ signatures of ejecta; e.g., Richardson & Cane, 1995), then the ICME ejecta boundaries would fall roughly between May 17, 2012 at 02:26 UT and May 19, 2012 at 06:59 UT (shaded region in Figure 12). This interval is consistent with MEX/MARSIS measurements, since the estimated trailing edge coincides with an increase in the crossing altitude, suggesting that the interplanetary transient had fully traveled past Mars. These boundaries would also place the leading edge ∼1 h after the May 17 flare onset and a few minutes after the arrival of energetic particles at Mars; however, since ASPERA-3 was not operational continuously at the time of these events, with gaps of a few hours between each observing session, the estimated boundaries are affected by large uncertainties. Nevertheless, it is reasonable to speculate that the SEP event onset and the passage of the ICME ejecta leading edge happened very close in time.

6. Discussion

In this section, we synthesize the multispacecraft observations, modeling results, and interpretations presented in Sections 3, 4 and 5 and discuss them in the context of three main topics: CME propagation across the inner heliosphere, CME magnetic structure, and CME role in SEP transport from the May 17, 2012 event.

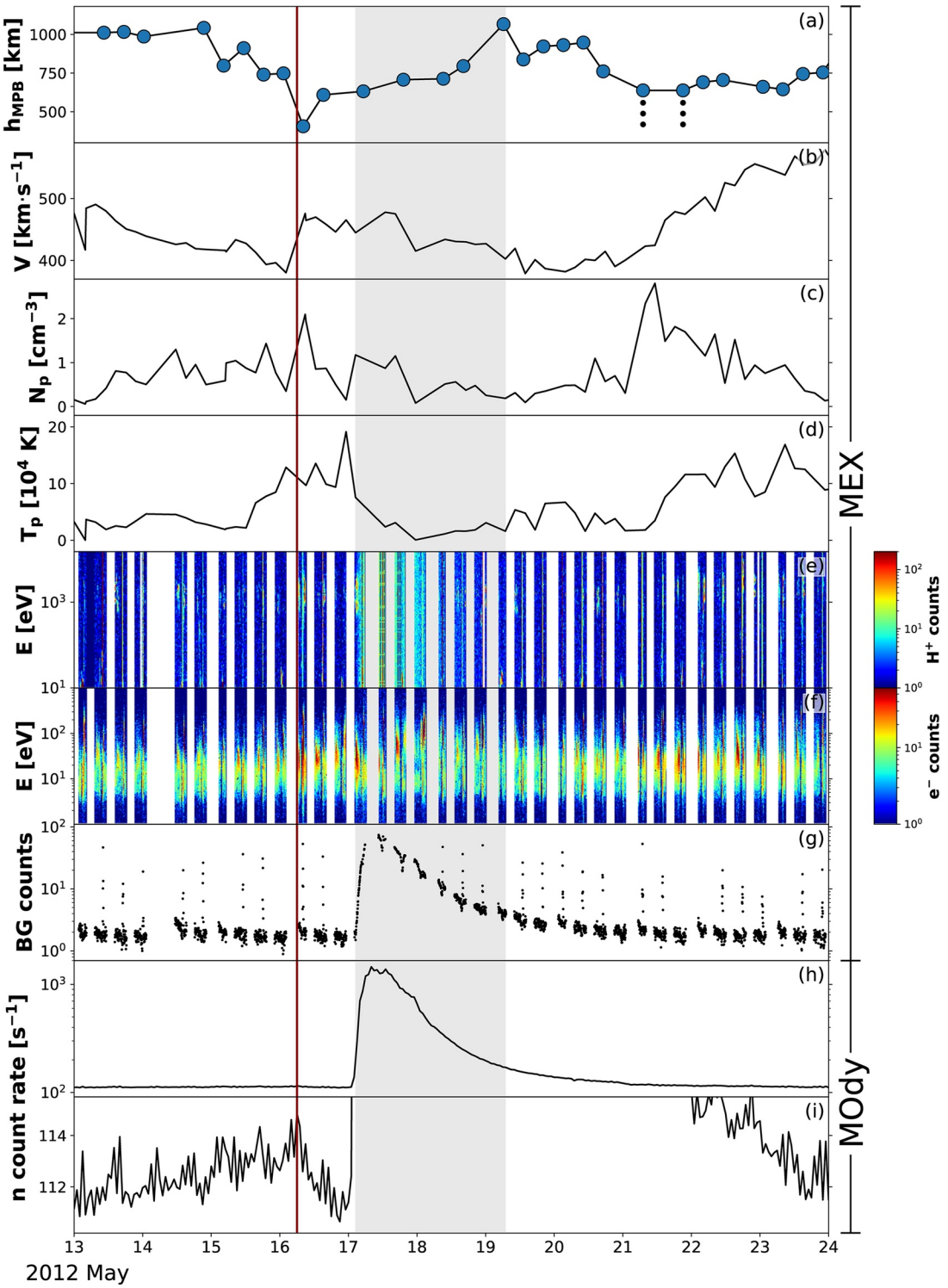

Figure 12. Measurements at Mars around the expected arrival time of the May 11, 2012 CME, revealing the passage of an interplanetary disturbance. Data are taken from (a–g) MEX and (h–i) MOdy. The solid vertical line indicates the arrival of the interplanetary shock, while the shaded area corresponds to the estimated ejecta interval. The parameters shown are: (a) altitude of the magnetic pileup boundary (inner boundary of the magnetosheath) outbound crossings for successive orbits, (b) solar wind speed, (c) proton density, (d) proton temperature, (e) proton and (f) electron energy distribution, (g) background counts, and (h–i) neutron counts per second. The three dots under two data points in panel (a) indicate that for those orbits only an upper limit for the crossing altitude could be estimated. Panel (i) is a zoomed-in version of the *y*–axis of panel (h). CME, coronal mass ejection; MEX, Mars Express; MOdy, Mars Odyssey.

6.1. CME Propagation

The May 11, 2012 eruption was a case of a CME experiencing moderate deflection very close to the Sun, with the CME source region being located at S13E13 on the disc (Section 3.1.1) and the CME propagation direction being S10E30 from GCS reconstructions in the corona (Section 3.1.2). This is not surprising, since most of the deflection is expected to take place below 30 $R_{\odot}$ from the Sun (Isavnin et al., 2014). CME deflections usually occur due to magnetic forces acting in the corona, which are dominant below 10 $R_{\odot}$ (e.g., Kay & Opher, 2015) and tend to divert CMEs toward the heliospheric current sheet and away from coronal holes (e.g., Cremades et al., 2006; Kilpua et al., 2009; Xie et al., 2009). In the case of the CME under study, the observed deflection can be likely attributed to two complementary factors, namely the global magnetic structure of the corona and the interchange reconnection scenario described in Section 3.1.1. Specifically, the CME source region was located at the edge between two highly inclined helmet streamers (from potential-field reconstructions, see Figure S4), and reconnection of the filament's eastern leg with the nearby open field resulted in the CME diverting toward the reconnection region (as shown in simulations by, e.g., Lugaz et al., 2011; Lynch & Edmondson, 2013; Török et al., 2011). We remark that such a deflection, despite being considered moderate, has in general important implications for space weather forecasting: if considering the location of the source region only, then one would expect a rather frontal encounter at Earth. Only through coronagraph observations did we estimate a flank encounter at Earth and a more central one at Mars (see Figure 1a), which was also the case for the January 7, 2014 CME studied by Möstl et al. (2015). In addition, CME deflections have also implications on the structure of the IMF, thus altering the longitudinal extent that will be available for SEP acceleration and detection.

Multispacecraft coronagraph and HI observations permitted us to evaluate the CME propagation direction and its half-angular extent in order to estimate its impact throughout the heliosphere using different propagation models (Section 4). If we exclude modeling results from the SSEF30-A technique reported in Table 1 (which can be considered as an outlier), then we can conclude that the arrival locations predicted by the models employed in this study were consistent with each other. However, despite the agreement in terms of hit/miss, the predicted arrival times throughout the inner heliosphere featured more substantial differences. This is mostly due to the physics and assumptions involved in each model. In fact, we note that the spread in arrival times increases with both heliocentric distance and angular separation from the CME nose. In the case of approximately central encounters, the major contribution to the spread is given by the physics that regulates the CME radial propagation in each model (constant acceleration for SSE/SSSE, drag-based with constant background for DBM, and MHD-based with variable background for Enlil). In the case of flank encounters, the major contribution to the spread is instead given by the geometry of the CME front assumed in each model (spherical cross-section for SSE/SSSE, circular arc for DBM, and evolving hydrodynamical structure for Enlil). Interestingly, we note that in the case of the SSSE model the CME is predicted to reach Mars before it reaches Earth, which is due to the perfectly circular shape of the CME front. In such cases, employing a larger CME half-width may solve the issue (a detailed study of how the SSSE model performs with respect to different CME half-widths is shown in Barnes et al., 2020). Furthermore, we remark that Palmerio et al. (2019) applied the (S)SSE model to two CMEs and noted that adding 15° to the GCS-derived half-width improved arrival time predictions in both cases. Nevertheless, employing several models with different assumptions can provide an overall context useful to interpret in-situ observations, as was demonstrated in this study.

A comparison of different modeling results with the in-situ observations presented in Section 5 is shown in Table 2. When considering differences between the predicted and measured arrival times, it is important to remark that all the forecasts reported in Section 4 were initiated using only remote-sensing data as input, and no adjustments were made to match in-situ observations. The propagation models were used as a guide to search for in-situ signatures, rather than to reproduce the observed arrivals. Most important, we remind the reader that we approximated the highly asymmetric and distorted May 11, 2012 CME with idealized, symmetrical structures in both coronagraph reconstructions (Section 3.1.2 and Figure 4) and propagation models (Section 4). Furthermore, apart from the well-known uncertainties in modeling CME arrival times that are estimated to be of the order of ±10 h at 1 AU regardless of the model used (e.g., Riley et al., 2018; Vourlidas et al., 2019; Wold et al., 2018), additional complications may arise from the preexisting solar wind conditions at the observing spacecraft. For example, the arrival times at Venus and Earth were likely

Table 2
CME Arrival Times From Three Modeling Techniques Presented in Section 4 Compared With the in-situ Observations presented in Section 5

Model	Venus	Earth	Spitzer	MSL	Mars
SSSE	05/14 19:15	05/17 18:51	05/15 15:01	05/17 00:13	05/17 14:57
DBM	05/14 00:08	05/15 00:20	05/14 23:42	05/16 14:42	05/17 05:49
Enlil (S)	05/13 19:33	05/14 21:30	05/14 20:03	05/16 05:54	05/16 21:58
Enlil (E)	05/14 01:00	05/15 17:52	05/15 21:07	05/17 03:06	05/17 23:27
Observed (S)	05/13 17:10	05/15 01:28	?	05/15 13:30	05/16 06:00
Observed (E)	05/14 19:23	05/16 15:57	?	?	05/17 02:26

Note. Dates are shown in the format MM/DD HH:MM. The notations "(S)" and "(E)" denote shock and ejecta, respectively. The question marks indicate that it is not possible to determine whether there has been an impact, and/or at what time.

affected by the preceding interplanetary structure (see Figures 8 and 9) that we attributed to an earlier, narrow eruption and that likely slowed down the May 11, 2012 ejecta. Furthermore, all the models predicted the impacts at MSL and Mars to take place significantly later than observed, which is possibly due to the faster wind preceding the CME at those heliolongitudes (see Figure 12). Taking all the aforementioned factors into account, these results suggest that, even in the case of particularly complex events, models that simplify their geometry could be used to satisfactorily estimate at least the impact location(s), albeit with sometimes significant errors in arrival times.

6.2. CME Magnetic Structure

The magnetic structure of the May 11, 2012 CME was inferred at several locations: at the Sun, through the solar corona, at Venus, and at Earth. The corresponding flux rope type was found to change dramatically across the different observation points. As shown in Section 3.1.1, the eruption of the May 11, 2012 CME involved the presence of a filament that disconnected asymmetrically from the Sun. The western leg stayed anchored to the photosphere for longer than the eastern one, which detached rapidly and resulted in a significant clockwise rotation of the filament. Based on these observations and on 3D reconstructions of the CME in the low corona (Figure 3), we estimated that the corresponding flux rope erupted as an ESW type, but was a NES type close to the Sun and a WNE type in the outer corona. The scenario of a filament eruption where one leg disconnects from the Sun early in the process while the other follows later was also observed by Vourlidas et al. (2011). The CME analyzed in their work erupted on June 16, 2010 featured negligible rotation below 3 $R_{\odot}$, but was observed in coronagraph imagery to rotate at an exceptionally fast rate, that is, 60°. In contrast, the May 11, 2012 CME studied here appeared to rotate significantly (~65°) already in the low corona. Both of these cases, however, feature the same outcome, that is, that the resulting magnetic configuration in the outer corona is significantly different from that at the Sun. These rapidly rotating events are particularly challenging for space weather forecasting of CME magnetic fields (e.g., Kilpua, Lugaz, et al., 2019), since information on the intrinsic flux rope type (inferred at the Sun) becomes practically obsolete.

Furthermore, the observed disconnection of one filament leg during the eruption raised questions about the evolution of the connectivity of the large-scale CME and whether the corresponding flux rope leg remained attached to the Sun. The relationship between the structure and evolution of erupting filaments and their overlying flux ropes is not always straightforward, and hence is an active area of research (e.g., Gibson & Fan, 2006; T. A. Howard et al., 2017; Schmieder et al., 2002). In the case of the event presented in this work, two main outcomes are possible: (1) the flux rope undergoes interchange reconnection together with the filament, hence completely detaching its western leg from the Sun, or (2) the large-scale flux rope (partially or in its entirety) maintains its field lines connected to the Sun, with the filament dynamics occurring at its periphery. We could not determine the connectivity of the flux rope from remote-sensing images alone, but measurements at Earth (Section 5.2) indicated the presence of bidirectional electrons during the first half of the ICME ejecta passage, suggesting that the front portion of the corresponding flux rope was still

attached to the Sun at both ends, while in the rear part at least one leg was disconnected. A similar PAD profile was reported by Nieves-Chinchilla et al. (2020), who analyzed a streamer-blowout flux rope that was observed by the Parker Solar Probe spacecraft on November 11–12, 2018. The authors provided three possible explanations for such a scenario: (1) a single (albeit distorted) flux rope transient, (2) a double flux rope, or (3) a combination of a flux rope and open magnetic field lines. Given the strong evidence for interchange reconnection presented in this work, known to be a common CME process (e.g., Crooker et al., 2002), we conclude that the latter option seems the most likely.

As we remarked in Section 3.1.2, the May 11, 2012 CME appeared significantly asymmetric and distorted in coronagraph imagery, especially from the SOHO and STEREO-B perspectives. Even though we approximated the CME morphology with a perfectly symmetrical GCS shell to derive its geometric and kinetic parameters (see Figure 4), it is important to keep in mind that the underlying flux rope may be considerably warped and that such deformations may be preserved or even enhanced in interplanetary space. Examples of deformed CME (and shock) fronts were reported by Farrugia et al. (2011), who found distortions and rotations in a magnetic cloud measured during November 19–21, 2007 by three spacecraft at 1 AU covering 40° in longitude, and Möstl et al. (2012), who found inconsistent flux rope inclinations with respect to the ecliptic plane in a series of CMEs launched on August 1, 2010 and measured at various locations in the inner heliosphere covering a 120° longitudinal span. From a space weather forecasting perspective, this means that knowledge of the global CME orientation at the Sun may have little to no correlation with the portion of CME that will be encountered in situ. More generally, Möstl et al. (2012) suggested that the orientation of a flux rope may be viewed as a local parameter, rather than a global one. It follows that it is especially difficult to distinguish between global rotations and local deformations of a flux rope, as was pointed out by Palmerio et al. (2018) who compared the orientations at the Sun with those at Earth for 20 CME events.

In interplanetary space, the magnetic structure of the May 11, 2012 CME could be evaluated at Venus (Section 5.1) and Earth (Section 5.2). The flux rope type and axis orientation resulted quite compatible when determined separately at the two locations but, in light of the aspects considered above, it is useful to evaluate whether the same holds true when regarding the ejecta as a coherent, rigid structure. In order to investigate this, we use the 3D Coronal Rope Ejection (3DCORE; Möstl et al., 2018; Weiss et al., 2021) modeling technique. 3DCORE is a forward simulation model that describes the structure of a CME using a torus-like geometry that is attached to the Sun and expands self-similarly as it propagates throughout the heliosphere. The expanding structure contains an embedded magnetic field that is based on an approximate analytical solution for torii (Vandas & Romashets, 2017) that is similar to a Gold-Hoyle (Gold & Hoyle, 1960; Farrugia et al., 1999) field. The fitting is performed using an approximate Bayesian computation sequential Monte Carlo algorithm, the implementation of which is described in detail in Weiss et al. (2021), that generates an ensemble of solutions. One significant advantage of this approach is that it is possible to estimate the errors on our parameters even if only using a single measurement. We initially proceed by applying the 3DCORE fitting algorithm to Wind measurements from Earth's L1 point, using boundary conditions that are very similar to those shown in Figure 9. The fit is evaluated on the interval spanning May 17, 2012 00:00 UT to 18:00 UT, using seven equidistant fitting points and a root-mean-square error metric. The overall time period in which ensemble solutions are accepted is set to May 16, 2012 16:00 UT, until May 17, 2012 22:30 UT. Figure 13a shows the reproduced flux rope signatures from the ensemble at Earth and the corresponding 2-σ spread in the magnetic field generated by the underlying uncertainties. We then back-propagate the obtained ensemble solution to Venus, allowing cross-verification of the Wind fit with the VEX measurements. This is achieved by simply re-running the simulations with the 3DCORE solution ensemble and moving the observer to Venus. The resulting magnetic field measurements from the ensemble solution at Venus, together with the propagated uncertainties, are shown in Figure 13b. Finally, we also show the 3D model structure of a representative ensemble sample from two different viewing angles (Figures 13c and 13d).

The results of the 3DCORE analysis suggest that the flux rope was oriented with a high inclination, up to 60° ± 10°, which is slightly larger than the result from the previous analysis (Sections 5.1 and 5.2), but nevertheless consistent with a WNE-to-SWN flux rope. Furthermore, the propagation direction of the CME is inferred to be on the opposite side of Earth when compared to the CME propagation results shown in Section 4 (see, e.g., Figure 7 for the Enlil simulation). In particular, these results predict a close miss at Mars, which is most likely not the case as there are in-situ measurements from MSL and the spacecraft orbiting

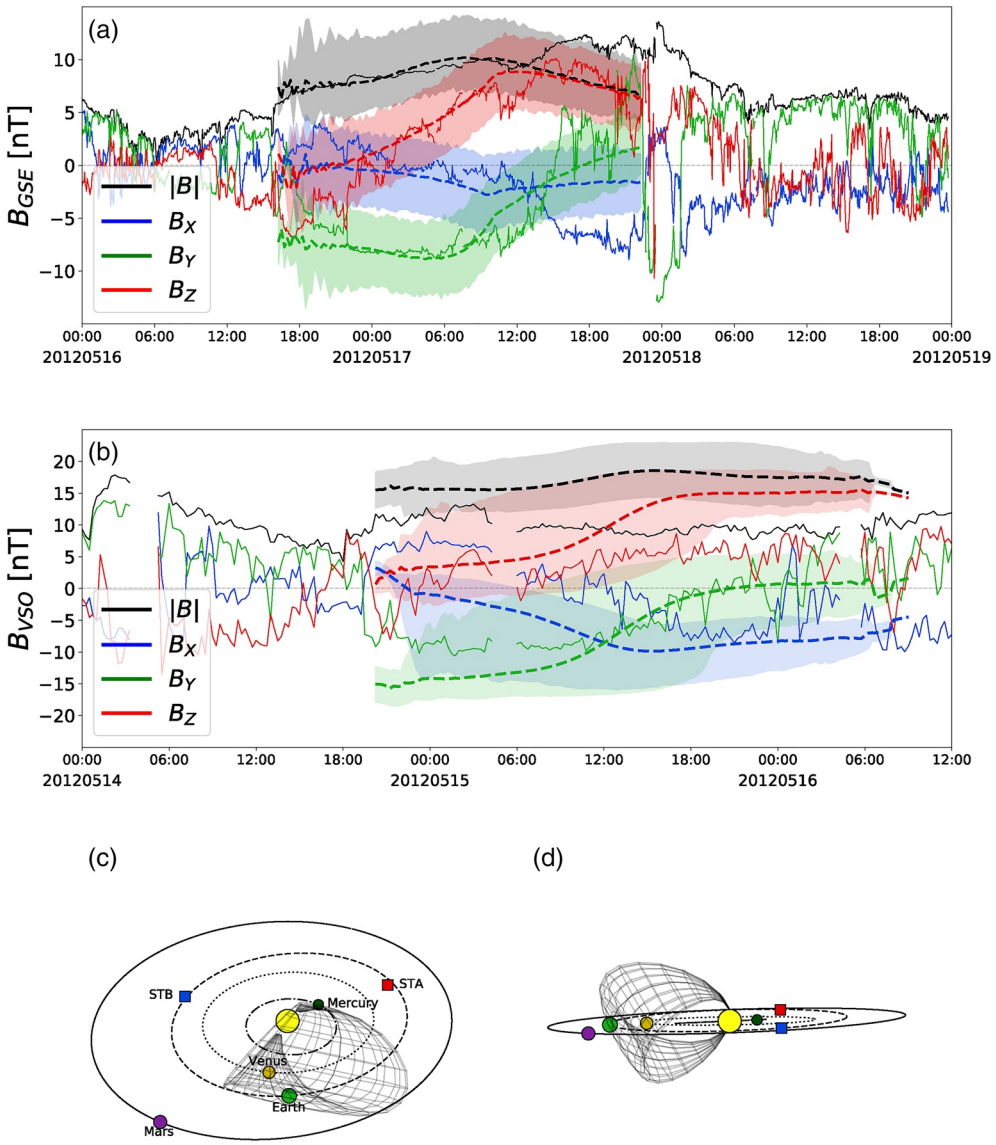

Figure 13. Modeling results from the 3DCORE analysis of the May 11, 2012 CME. (a) 3DCORE ensemble fit of the ICME ejecta at Earth using measurements from Wind. (b) The fit shown in panel (a) back-propagated to Venus and superposed on VEX measurements. (c–d) Visualization of the CME structure resulting from 3DCORE for a representative ensemble sample. 3DCORE, 3D Coronal Rope Ejection; CME, coronal mass ejection; VEX, Venus Express.

Mars that strongly hint toward the contrary. These types of disagreements, however, are not out of the ordinary, as we have only fitted the in-situ magnetic field measurements at Earth's L1 point and have not added any additional constraints from other positions. Furthermore, these discrepancies may be related to CME distortion during transit and to how coherent the internal MHD structure of CMEs remains beyond ~0.3 AU from the Sun (Owens et al., 2017).

Figure 13a shows that we are able to largely reconstruct the measured magnetic field profile using the 3DCORE model. The only larger discrepancy can be found in the B_X component toward the end of the flux rope. Further assessment on the quality of this fit can be obtained by cross-verifying our results with measurements at Venus. In Figure 13b, for simplicity, we only show the mean back-propagated ensemble of our solution at the position of the VEX spacecraft. We can conclude that, in general, the back-propagated and measured flux ropes are more or less in qualitative agreement. There is a big difference with respect to the

total magnetic field strength, which can be attributed to the scaling relations that are implemented in the model. When compensating for this, the only large remaining discrepancy is again the B_X component. As the VSO coordinate system is essentially the GSE equivalent for Venus, and at the time point of interest Venus and Earth are almost radially aligned, this can be expected from the same B_X discrepancy at Earth. This shows that, at least to the first order, the measurements at Venus and Earth are consistent with each other and do not show any drastic evolution, clearly demonstrating that the same ICME flux rope was observed at both planets.

In conclusion, the direction of the May 11, 2012 flux rope axis was found to rotate by at least ∼180° clockwise between the Sun and Venus, highlighting the difficulties for space weather forecasting of the B_Z component for rapidly rotating events. In particular, at least ∼55° of this rotation seems to have taken place between the last coronagraph observation and Venus, in agreement with Isavnin et al. (2014) who reported that a significant amount of CME deflection and rotation can still happen between 30 $R_\odot$ and 1 AU. However, we remark that, in light of the discussion above, CME rotation might have been extreme at the longitudes of Venus and Earth but not at other locations, for example, at Mars, where the flux rope type could not be determined. In this regard, it is worth mentioning that the rotating CME analyzed in the solar corona by Vourlidas et al. (2011) was then analyzed from the Sun to Earth by Nieves-Chinchilla et al. (2012), passing by Mercury that was separated by ∼20°from the Sun–Earth line. The authors found significant discrepancies in the flux rope tilt between observations in the solar corona and those at Mercury (by ∼100°) and then from Mercury to Earth (between 20° and 50° depending on the chosen flux rope boundaries). The results presented in Nieves-Chinchilla et al. (2012) and in this work show the importance of having magnetic field measurements of the same ICME at widely longitudinally separated spacecraft, in order to discern between global rotations and local distortions.

6.3. CME Role in SEP Transport

One key aim of this work was to explore the effect of the May 11, 2012 CME on the observed profiles of the SEP event that originated from the May 17, 2012 eruption. SEP signatures were indeed observed at all the locations that were predicted to be encountered by the May 11 CME (Section 4), that is, Venus, Earth, Spitzer, MSL, and Mars. These findings suggest that the required magnetic connectivity for the impulsive characteristics of the in situ SEPs was provided by the May 11 ICME, which was likely crossing all the five in situ locations (Section 5) where SEP signatures were detected. This was also the conclusion drawn by Rouillard et al. (2016) based on in situ measurements at Earth only. In order to further explore this hypothesis, we first check whether SEP signatures were observed at other locations in the inner heliosphere, that is, Mercury and the two STEREO spacecraft (see Figure 1b). Measurements from these three points were analyzed by Battarbee et al. (2018, see also Figure 14), who reported the presence of a gradual event at all observers, hence confirming that fast-spreading, rapidly rising SEP profiles were detected only at those locations that were being encompassed by the May 11 ICME.

Figures 14a and 14b illustrates the May 17, 2012 SEP transport scenario with and without the presence of the May 11, 2012 CME. The flare site and all planets and spacecraft in the inner heliosphere have been connected through Parker spiral (Parker, 1958) field lines for a solar wind speed of 400 kms^{-1} in Figure 14a. As this is a hypothetical situation, we have chosen the speed of 400 kms^{-1} to be representative of typical slow solar wind conditions close to the solar equatorial plane. It is clear from the illustration that no spacecraft in the inner heliosphere would have been perfectly magnetically connected to the eruption source region under these conditions. The longitudinal separation between the flare site and the spiral line footpoints of the locations where SEPs were observed spans from ∼15° (Earth) to ∼85° (Spitzer). The best connectivity to Earth, MSL, and Mars would be achieved for solar wind speeds in the range 310–340 kms^{-1}, while the best connectivity to Venus and Spitzer would be achieved for speeds in the range 170–200 kms^{-1}. Realistically speaking, it seems highly unlikely for each of these locations to be simultaneously connected to the eruptive region, which is the reason why more impulsive SEP events are usually observed over a spatially narrow region compared to gradual ones. One way to provide simultaneous connectivity to all observers would be the passage of the ICME ejecta associated with the May 11, 2012 CME, illustrated in Figure 14b. On May 17, 2012 at 01:30 UT, the source region of the May 11 CME had rotated to S13W57, hence was in the vicinity (within ∼20° in both latitude and longitude) of the source region of the May 17 CME (N11W76). In such

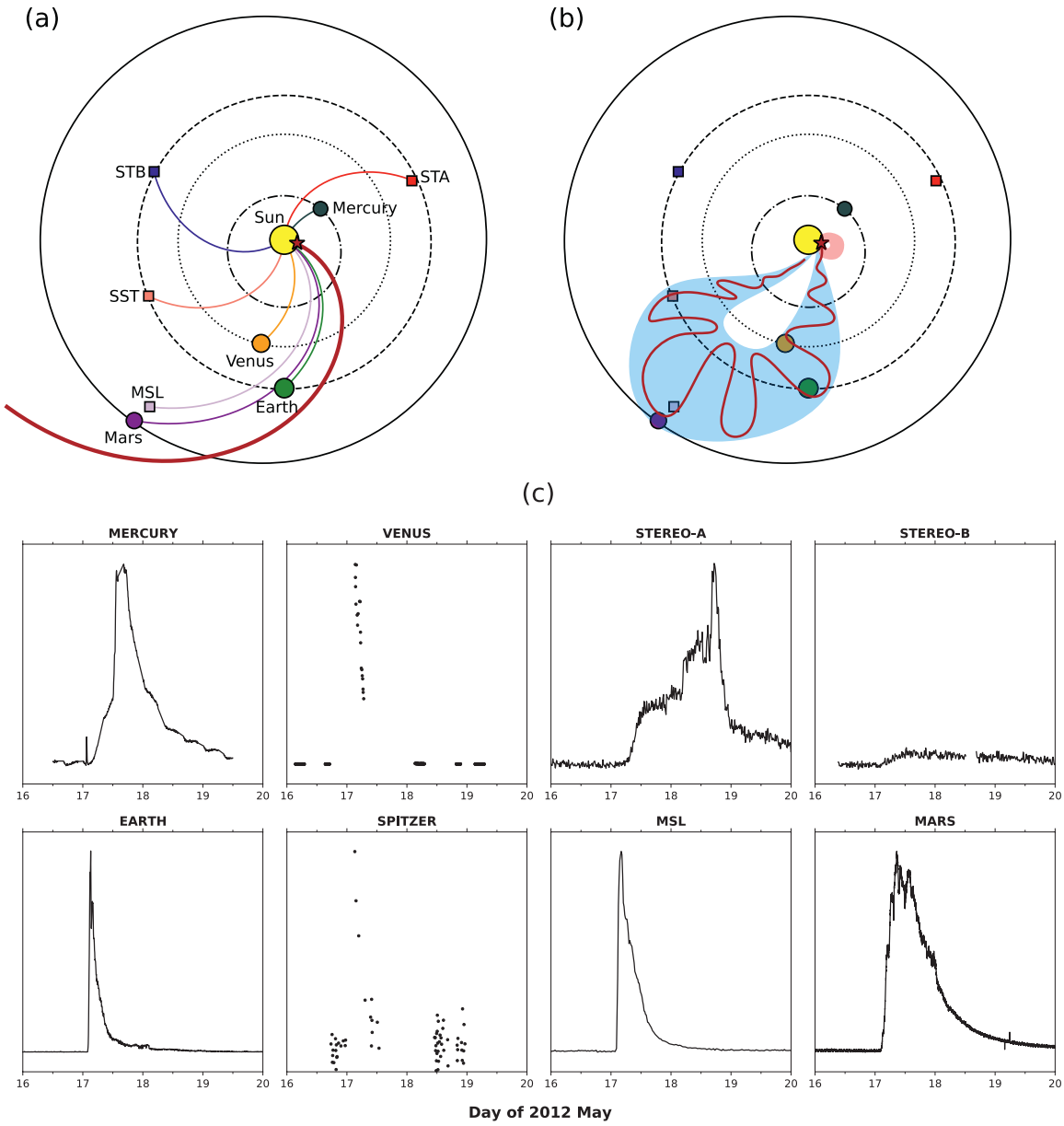

Figure 14. The May 17, 2012 SEP event throughout the inner heliosphere. (a and b) Schematic to illustrate the scenario of the May 11, 2012 CME and the May 17, 2012 SEP event in the inner heliosphere. The flaring site (N11W76) is indicated with a star symbol on the edge of the circle representing the Sun. The configuration of the various planets and spacecraft is the same as in Figure 1b. (a) Hypothetical SEP transport scenario in the absence of the May 11 CME. All planets and spacecraft in the inner heliosphere have been connected to the Sun through the nominal Parker spiral for a solar wind speed of 400 kms^{-1}. The same spiral is streaming from the flare location and is represented with a thicker line. (b) The SEP transport scenario in the presence of the May 11 CME (shaded in blue) and the May 17 CME (shaded in red). SEPs propagate along the field lines within the magnetic ejecta of the May 11 CME. Connectivity to Mercury and the twin STEREO spacecraft is not shown. (c) SEP profiles (in linear scale) at all the in situ locations shown in panels (a and b). All measurements are normalized and shown in arbitrary units, apart from STEREO-B measurements that are normalized to the STEREO-A ones. The approximate minimum energies that each shown data set is sensitive to are: 15 MeV at MESSENGER, 14 MeV at STEREO, 30 MeV at GOES, 100 MeV at Spitzer (Cheng et al., 2014), 35 MeV at MSL (Zeitlin et al., 2013), and 0.2 MeV at MOdy (Sánchez-Cano et al., 2018). The minimum energy range for VEX is unknown, but it can be approximated to be similar to that of MEX (20 MeV for protons), which was derived by Ramstad et al. (2018) via cross-calibration with measurements from the Mars Atmosphere and Volatile Evolution (MAVEN) spacecraft. CME, coronal mass ejection; GOES, Geostationary Operational Environmental Satellites; MESSENGER, Mercury Surface, Space Environment, Geochemistry, and Ranging; MEX, Mars Express; MOdy, Mars Odyssey; MSL, Mars Science Laboratory; SEP, solar energetic particle; STEREO, Solar Terrestrial Relations Observatory; VEX, Venus Express.

a scenario, the shock driven by the May 17 CME in the low corona (which was estimated by Gopalswamy et al., 2013, to have formed at 1.38 $R_{\odot}$) would easily intersect the western leg of the May 11 CME and accelerated particles would rapidly propagate throughout the magnetic ejecta. The energization process itself is expected to take place on particles that are already within the May 11 CME flank, but additional SEPs could be introduced into the leg via direct or indirect transport processes such as magnetic reconnection or cross-field diffusion.

Figure 14c shows the SEP profiles from the 2012 May 17 eruption measured in situ at eight different locations in the inner heliosphere. This makes it one of the SEP events that have been most widely observed by spacecraft at different locations. As pointed out by Battarbee et al. (2018), Mercury and STEREO-A observed a slowly rising SEP profile. Both locations did also measure the passage of an ICME: the one at Mercury (between 12:10 and 15:39 UT on May 17) was reported by Winslow et al. (2015), while the one at STEREO-A (between May 18 at 12:43 UT and May 19 at 09:12 UT) can be found in the STEREO ICME list (Jian et al., 2018). The peak speed of 840 kms^{-1} measured at STEREO-A is consistent with the fast May 17 CME. The gradual SEP profile at Mercury and STEREO-A is followed by an additional population of energetic storm particles (ESPs) upon the arrival of the ICME-driven shock, suggesting that particles were locally accelerated at the shock as it propagated through interplanetary space. Furthermore, STEREO-B observed a weak increase in proton flux. Such increase may be related to the May 17 CME or, alternatively, may stem from other mechanisms such as drift motion, corotation, cross-field diffusion, and turbulence (as suggested by Battarbee et al., 2018). We point out that the large extent and high speed of the May 17, 2012 CME, together with the other possible mechanisms enumerated above, do not rule out the fact that SEPs may have been measured at all eight locations without the presence of the May 11 CME, but it is likely that at least some of them would have experienced more slowly rising profiles such as those seen at Mercury and STEREO-A. The impulsive SEP profiles observed at Venus, Earth, Spitzer, MSL, and Mars suggest that an "instantaneous" connectivity was established through the May 11 CME, which does not exclude that a connectivity may have been established via other means. For instance, a later connection to the wide-extent and outward propagating shock of the May 17 event could also be possible for observers to the west of the event source (e.g., Lario et al., 2017).

One interesting aspect to consider in the framework of IMF connectivity is the path length traveled by energetic particles up to the locations encompassed by the May 11 CME. If SEPs propagate through the preceding ejecta rather than the nominal Parker spiral, then such lengths can be expected to present somewhat higher values than "normal." In the case under study, this analysis cannot be performed for Venus and Spitzer, where SEPs were first detected after 03:00 UT on May 17, 2012 due to data gaps. Continuous measurements at Earth, MSL, and Mars, on the other hand, enabled us to estimate precise onset times for the SEP event (01:56 UT, 02:04 UT, and 02:16 UT, respectively). These times were estimated using the Poisson-CUSUM (Lucas, 1985) method, which has been widely employed in the case of SEP events (e.g., Huttunen-Heikinmaa et al., 2005; Xu et al., 2020). Assuming 1 GeV protons (which can be considered an upper energy limit for this event; e.g., Kühl et al., 2015), a particle release time of 01:39 UT (consistent with the results in Gopalswamy et al., 2013; Li et al., 2013), and uniform acceleration efficiency, the SEP onset times at the three locations would yield path lengths of 1.79 AU at Earth, 2.63 AU at MSL, and 3.89 AU at Mars. These values are all significantly higher than the corresponding Parker spiral lengths shown in Figure 14a (1.18 AU at Earth, 1.91 AU at MSL, and 2.25 AU at Mars), thus suggesting that connectivity was not achieved through the nominal IMF but instead via the May 11 CME ejecta. Furthermore, the path length at Earth (1.79 AU) is consistent with the one derived by Rouillard et al. (2016), that is 1.89 AU. The large difference between the path lengths at MSL (2.63 AU) and Mars (3.89 AU), when the two locations where separated by only ~0.2 AU, may be explained by the almost simultaneous arrival at Mars of the May 17 SEP event and the May 11 ejecta leading edge, as was shown in Section 5.5. On one hand, it is possible that optimal connectivity was reached slightly later at Mars; on the other hand, Mars might have been magnetically connected to the outer (helical) flux rope fields of the May 11 CME, which in Lunquist-like (e.g., Lepping et al., 1990; Lundquist, 1950) models present the highest degree of twist, hence resulting in a longer path length.

It is not unheard that SEPs can arrive at an observer from source regions that would be considered poorly to not connected. Apart from Rouillard et al. (2016) who analyzed the same event described here, Masson

et al. (2012) studied 10 GLE events between 2000 and 2006 and concluded that only three of them are consistent with particle propagation under nominal Parker spiral conditions. Five of these events occurred during the passage of CME-related disturbances past the spacecraft observing the SEPs, that is sheath regions, magnetic clouds, or ejecta rear regions, suggesting that regions on the Sun that would not otherwise be magnetically connected to Earth may be temporarily connected through transient magnetic structures. Furthermore, Dresing et al. (2016) reported observations of an impulsive electron event on November 7, 2013 at both STEREO spacecraft, which were separated by 68° in longitude. While STEREO-A was well connected with respect to the flaring region, connectivity at STEREO-B was shown to be due to the passage of a CME that erupted three days earlier from the same source region. Indeed, as mentioned in the Introduction, observations of impulsive SEPs over large longitudinal ranges are widely documented in the literature but, to our knowledge, this is the first time that SEP transport inside a preceding ICME has been observed at five well-separated locations, distributed over 70° in longitude and at four heliocentric distances between 0.7 and 1.6 AU. It is important to consider the space weather implications of such a scenario: first, Gopalswamy et al. (2013) noted that the May 17, 2012 flare size (M5.1) was rather small for having resulted in a GLE event. One possible interpretation for the unexpected acceleration of SEPs to high energies is the twin-shock and/or twin-acceleration scenario discussed by Shen et al. (2013) and Ding et al. (2016). However, the observations herein discussed are also consistent with the findings of Lario & Karelitz (2014), who demonstrated that SEP events observed within preceding ICMEs tend to show higher peak intensities than those observed in the undisturbed solar wind. Second, the 2012 May 11 CME was observed at Earth as a rather slow event with almost no negative B_Z, hence its geoeffectiveness was very modest (it was associated with a $\mathrm{Dst}_{\mathrm{min}} = -43$ nT). Yet, its passage enabled observations of the first GLE event of solar cycle 24, and could have possibly represented the first GLE measured on the surface of two planets had Curiosity already landed on Mars (the "record" went later to the September 10, 2017 event studied by, for example, Guo et al., 2018; Hassler et al., 2018; Lee et al., 2018; Zeitlin et al., 2018).

7. Conclusions

In this work, we have followed the eruption and evolution of the May 11, 2012 CME and its role in spreading SEPs that originated from a later eruption on May 17, 2012. After analyzing the May 11, 2012 event using remote-sensing imagery of the solar disc, corona, and inner heliosphere, we have estimated its impact throughout interplanetary space using several propagation models. Then, we have searched for signatures of the CME passage at each of the five predicted impact locations (i.e., Venus, Earth, Spitzer, MSL, and Mars). Where possible, we have studied well-known properties and phenomena usually associated with ICMEs, such as the magnetic field configuration and the associated Forbush decrease. After finding nearly simultaneous SEP signatures at all five in-situ locations, we suggested that energetic particles accelerated by the May 17, 2012 eruption could spread over a large range of heliolongitudes due to the magnetic connectivity provided by the May 11 CME.

This work highlights the importance of using data from multiple viewpoints, both from a remote-sensing and an in-situ perspective, to characterize the complex evolution of CMEs. The event under study here appeared to be significantly distorted and rapidly rotating, which may explain why the magnetic configuration of the corresponding flux rope was not consistent across all the observation points. Some of the spacecraft employed in this study are no longer operational (e.g., MESSENGER, VEX, Spitzer, and STEREO-B), but several new missions are currently available (e.g., Parker Solar Probe, Solar Orbiter, BepiColombo, and MAVEN). Coordinated observations that employ multiple spacecraft and ground facilities will be beneficial to our understanding of CME physics, from their eruption through their interplanetary journey. International efforts such as the Whole Heliosphere and Planetary Interactions (WHPI; https://whpi.hao.ucar.edu) initiative, which aims to coordinate observations and modeling of the solar–heliospheric–planetary system during solar minimum, or the planned coordinated campaigns between Parker Solar Probe and Solar Orbiter (Velli et al., 2020), are the needed step forward toward a better understanding of these complex processes.

Finally, this work showed how the interplanetary impact of the SEPs associated with the May 17, 2012 eruptive flare was tremendously influenced by the presence of the preceding May 11 ICME in the inner heliosphere. The IMF connectivity to the flare/shock acceleration site is a critical component for estimating the severity and potential impact of impulsive SEPs. While these events tend to be relatively narrow in

Acknowledgments
E. Palmerio acknowledges the Doctoral Programme in Particle Physics and Universe Sciences (PAPU) at the University of Helsinki, the Emil Aaltonen Foundation, and the NASA Living With a Star Jack Eddy Postdoctoral Fellowship Program, administered by UCAR's Cooperative Programs for the Advancement of Earth System Science (CPAESS) under award no. NNX-16AK22G. E. Kilpua acknowledges the SolMAG project (ERC-COG 724391) funded by the European Research Council (ERC) in the framework of the Horizon 2020 Research and Innovation Programme, Academy of Finland project SMASH (grant no. 310445), and the Finnish Centre of Excellence in Research of Sustainable Space (Academy of Finland grant no. 312390). B. Sánchez-Cano acknowledges support through UK-STFC grant ST/S000429/1. A. Weiss and C. Möstl thank the Austrian Science Fund (FWF): P31521-N27. M. Mierla, A. Zhukov, and L. Rodriguez thank the European Space Agency (ESA) and the Belgian Federal Science Policy Office (BELSPO) for their support in the framework of the PRODEX Programme. J. Guo thanks the Strategic Priority Program of the Chinese Academy of Sciences (grant no. XDB41000000 and XDA15017300), and the CNSA preresearch Project on Civil Aerospace Technologies (grant no. D020104). The work of L. Turc is supported by the Academy of Finland (grant no. 322544). We thank two anonymous reviewers, whose comments and suggestions have significantly improved this article. We acknowledge support from the European Union FP7-SPACE-2013-1 programme for the HELCATS project (grant no. 606692). The HI instruments on STEREO were developed by a consortium that comprised the Rutherford Appleton Laboratory (UK), the University of Birmingham (UK), Centre Spatial de Liège (CSL, Belgium) and the Naval Research Laboratory (NRL, USA). The STEREO/SECCHI project, of which HI is a part, is an international consortium led by NRL. We recognize the support of the UK Space Agency for funding STEREO/HI operations in the UK. The WSA model was developed by C. N. Arge (currently at NASA/GSFC), and the Enlil model was developed by D. Odstrcil (currently at GMU). We thank the model developers, M. L. Mays, R. Colaninno, and the CCMC staff. We acknowledge the NMDB, founded under the European Union's FP7 programme (contract no. 213007), for providing neutron monitor data. We thank the WDC for Geomagnetism, Kyoto, and the geomagnetic observatories for their cooperation to make the final Dst indices available. This work is based (in part) on archival data obtained with

longitudinal extent, we have shown the May 17, 2012 event was seen nearly simultaneously at five separate locations (three of which were planets) separated by up to ∼150° in heliographic longitude from the flaring region. Therefore, an instantaneous extrapolation of the magnetic field configuration of the flare/eruption site may not be sufficient to estimate the actual spatial extent of impulsive SEP events—the temporal history of the coronal and heliospheric field structure and evolution can also play an important role in the preconditioning of the IMF necessary for extreme events.

Data Availability Statement

The HELCATS catalogs are available at https://www.helcats-fp7.eu. Images and additional information on the May 12, 2012 CME are available at https://www.helcats-fp7.eu/catalogues/event_page.html?id=HCME_A__20120511_01 (STEREO-A viewpoint) and https://www.helcats-fp7.eu/catalogues/event_page.html?id=HCME_B__20120512_01 (STEREO-B viewpoint). The WSA–Enlil + Cone simulation results have been provided by the Community Coordinated Modeling Center (CCMC) at NASA Goddard Space Flight Center through their public Runs on Request system (http://ccmc.gsfc.nasa.gov). The full simulation results are available at https://ccmc.gsfc.nasa.gov/database_SH/Erika_Palmerio_093020_SH_1.php. The Richardson & Cane ICME list is available at http://www.srl.caltech.edu/ACE/ASC/DATA/level3/icmetable2.htm, while the NASA–Wind ICME list can be found at https://wind.nasa.gov/ICMEindex.php. Solar disc and coronagraph data from SDO, SOHO, and STEREO are openly available at the Virtual Solar Observatory (VSO; https://sdac.virtualsolar.org/). These data were processed and analyzed through SunPy (SunPy Community et al., 2015, 2020), IDL SolarSoft (Bentely & Freeland, 1998), and the ESA JHelioviewer software (Müller et al., 2017). Level-2 processed STEREO/HI data were obtained from the UK Solar System Data Centre (UKSSDC; https://www.ukssdc.ac.uk/solar/stereo/data.html). GOES/XRS data were retrieved from https://sohoftp.nascom.nasa.gov. VEX and MEX data are openly available at ESA's Planetary Science Archive (https://archives.esac.esa.int/psa). These data were processed and analyzed with the aid of the irfpy library (https://irfpy.irf.se/irfpy/index.html). Wind data are publicly available at NASA's Coordinated Data Analysis Web (CDAWeb) database (https://cdaweb.sci.gsfc.nasa.gov/index.html/). Energetic particle data from GOES can be accessed at https://www.ngdc.noaa.gov/stp/satellite/goes/. NMDB data are publicly available at http://www.nmdb.eu and Dst data can be found at http://wdc.kugi.kyoto-u.ac.jp/wdc/Sec3.html. Spitzer data are available at the NASA/IPAC Infrared Science Archive (https://irsa.ipac.caltech.edu/). MSL data are openly available at the Planetary Plasma Interactions (PPI) Node of NASA's Planetary Data System (PDS), accessible at https://pds-ppi.igpp.ucla.edu. MOdy and MESSENGER data are available at the Geosciences Node of the PDS, accessible at https://pds-geosciences.wustl.edu/. STEREO/HET data were accessed at http://www.srl.caltech.edu/STEREO/Public/HET_public.html. The STEREO ICME list can be found at https://stereo-ssc.nascom.nasa.gov/pub/ins_data/impact/level3/STEREO_Level3_ICME.pdf.

References

Al-Haddad, N., Nieves-Chinchilla, T., Savani, N. P., Möstl, C., Marubashi, K., Hidalgo, M. A., et al. (2013). Magnetic field configuration models and reconstruction methods for interplanetary coronal mass ejections. *Solar Physics*, *284*, 129–149. https://doi.org/10.1007/s11207-013-0244-5

Amerstorfer, T., Möstl, C., Hess, P., Temmer, M., Mays, M. L., Reiss, M. A., et al. (2018). Ensemble prediction of a halo coronal mass ejection using heliospheric imagers. *Space Weather*, *16*(7), 784–801. https://doi.org/10.1029/2017SW001786

Anastasiadis, A., Lario, D., Papaioannou, A., Kouloumvakos, A., & Vourlidas, A. (2019). Solar energetic particles in the inner heliosphere: Status and open questions. *Philosophical Transactions of the Royal Society of London, Series A*, *377*(2148), 20180100. https://doi.org/10.1098/rsta.2018.0100

Arge, C. N., Luhmann, J. G., Odstrcil, D., Schrijver, C. J., & Li, Y. (2004). Stream structure and coronal sources of the solar wind during the May 12th, 1997 CME. *Journal of Atmospheric and Solar-Terrestrial Physics*, *66*, 1295–1309. https://doi.org/10.1016/j.jastp.2004.03.018

Baker, D., Rouillard, A. P., van Driel-Gesztelyi, L., Démoulin, P., Harra, L. K., Lavraud, B., et al. (2009). Signatures of interchange reconnection: STEREO, ACE and Hinode observations combined. *Annales Geophysicae*, *27*(10), 3883–3897. https://doi.org/10.5194/angeo-27-3883-2009

Barabash, S., Lundin, R., Andersson, H., Brinkfeldt, K., Grigoriev, A., Gunell, H., et al. (2006). The Analyzer of Space Plasmas and Energetic Atoms (ASPERA-3) for the Mars Express mission. *Space Science Reviews*, *126*, 113–164. https://doi.org/10.1007/s11214-006-9124-8

Barabash, S., Sauvaud, J.-A., Gunell, H., Andersson, H., Grigoriev, A., Brinkfeldt, K., et al. (2007). The Analyser of Space Plasmas and Energetic Atoms (ASPERA-4) for the Venus Express mission. *Planetary and Space Science*, *55*, 1772–1792. https://doi.org/10.1016/j.pss.2007.01.014

Barnes, D., Davies, J. A., Harrison, R. A., Byrne, J. P., Perry, C. H., Bothmer, V., et al. (2019). CMEs in the heliosphere: II. A statistical analysis of the kinematic properties derived from single-spacecraft geometrical modelling techniques applied to CMEs detected in the heliosphere from 2007 to 2017 by STEREO/HI-1. *Solar Physics*, *294*(5), 57. https://doi.org/10.1007/s11207-019-1444-4

the Spitzer Space Telescope, which was operated by the Jet Propulsion Laboratory, California Institute of Technology, under a contract with NASA. Support for this work was provided by an award issued by JPL/Caltech. Finally, we thank the instrument teams of all the spacecraft involved in this study.

Barnes, D., Davies, J. A., Harrison, R. A., Byrne, J. P., Perry, C. H., Bothmer, V., et al. (2020). CMEs in the heliosphere: III. A statistical analysis of the kinematic properties derived from stereoscopic geometrical modelling techniques applied to CMEs detected in the heliosphere from 2008 to 2014 by STEREO/HI-1. *Solar Physics*, *295*(11), 150. https://doi.org/10.1007/s11207-020-01717-w

Battarbee, M., Guo, J., Dalla, S., Wimmer-Schweingruber, R., Swalwell, B., & Lawrence, D. J. (2018). Multi-spacecraft observations and transport simulations of solar energetic particles for the May 17th 2012 event. *Astronomy & Astrophysics*, *612*, A116. https://doi.org/10.1051/0004-6361/201731451

Bemporad, A., Mierla, M., & Tripathi, D. (2011). Rotation of an erupting filament observed by the STEREO EUVI and COR1 instruments. *Astronomy & Astrophysics*, *531*, A147. https://doi.org/10.1051/0004-6361/201016297

Bentely, R. D., & Freeland, S. L. (1998). SOLARSOFT-an analysis environment for solar physics. In *Crossroads for European solar and heliospheric physics. Recent achievements and future mission possibilities* (Vol. *417*, pp. 225).

Benz, A. O. (2017). Flare observations. *Living Reviews in Solar Physics*, *14*, 2. https://doi.org/10.1007/s41116-016-0004-3

Berrilli, F., Casolino, M., Del Moro, D., Di Fino, L., Larosa, M., Narici, L., et al. (2014). The relativistic solar particle event of May 17th, 2012 observed on board the International Space Station. *Journal of Space Weather and Space Climate*, *4*, A16. https://doi.org/10.1051/swsc/2014014

Bobra, M. G., Sun, X., Hoeksema, J. T., Turmon, M., Liu, Y., Hayashi, K., et al. (2014). The helioseismic and magnetic imager (HMI) vector magnetic field pipeline: SHARPs - space-weather HMI active region patches. *Solar Physics*, *289*, 3549–3578. https://doi.org/10.1007/s11207-014-0529-3

Bothmer, V., & Schwenn, R. (1998). The structure and origin of magnetic clouds in the solar wind. *Annales Geophysicae*, *16*, 1–24. https://doi.org/10.1007/s00585-997-0001-x

Boynton, W. V., Feldman, W. C., Mitrofanov, I. G., Evans, L. G., Reedy, R. C., Squyres, S. W., et al. (2004). The Mars Odyssey gamma-ray spectrometer instrument suite. *Space Science Reviews*, *110*, 37–83. https://doi.org/10.1023/B:SPAC.0000021007.76126.15

Brueckner, G. E., Howard, R. A., Koomen, M. J., Korendyke, C. M., Michels, D. J., Moses, J. D., et al. (1995). The large angle spectroscopic coronagraph (LASCO). *Solar Physics*, *162*, 357–402. https://doi.org/10.1007/BF00733434

Cane, H. V. (2000). Coronal mass ejections and Forbush decreases. *Space Science Reviews*, *93*, 55–77. https://doi.org/10.1023/A:1026532125747

Cane, H. V., McGuire, R. E., & von Rosenvinge, T. T. (1986). Two classes of solar energetic particle events associated with impulsive and long-duration soft X-ray flares. *The Astrophysical Journal*, *301*, 448. https://doi.org/10.1086/163913

Cane, H. V., & Richardson, I. G. (2003). Interplanetary coronal mass ejections in the near-Earth solar wind during 1996-2002. *Journal of Geophysical Research*, *108*(A4), 1156. https://doi.org/10.1029/2002JA009817

Cane, H. V., Richardson, I. G., & von Rosenvinge, T. T. (2010). A study of solar energetic particle events of 1997-2006: Their composition and associations. *Journal of Geophysical Research*, *115*(A8), A08101. https://doi.org/10.1029/2009JA014848

Cheng, L. Y., Hunt, J. C. J., Stowers, K., Lowrance, P., Steward, A., & Travis, P. (2014). Investigating space weather events impacting the spitzer space telescope. In *Spaceops Conferences*. https://doi.org/10.2514/6.2014-1910

Chicarro, A., Martin, P., & Trautner, R. (2004). The Mars Express mission: An overview. In A. Wilson, & A. Chicarro (Eds.), Mars Express: The scientific payload (Vol. 1240, pp. 3–13). European Space Agency Special Publication.

Cremades, H., Bothmer, V., & Tripathi, D. (2006). Properties of structured coronal mass ejections in solar cycle 23. *Advances in Space Research*, *38*(3), 461–465. https://doi.org/10.1016/j.asr.2005.01.095

Crooker, N. U., Gosling, J. T., & Kahler, S. W. (2002). Reducing heliospheric magnetic flux from coronal mass ejections without disconnection. *Journal of Geophysical Research*, *107*(A2), 1028. https://doi.org/10.1029/2001JA000236

Davies, J. A., Harrison, R. A., Perry, C. H., Möstl, C., Lugaz, N., Rollett, T., et al. (2012). A self-similar expansion model for use in solar wind transient propagation studies. *The Astrophysical Journal*, *750*, 23. https://doi.org/10.1088/0004-637X/750/1/23

Davies, J. A., Harrison, R. A., Rouillard, A. P., Sheeley, N. R., Perry, C. H., Bewsher, D., et al. (2009). A synoptic view of solar transient evolution in the inner heliosphere using the Heliospheric Imagers on STEREO. *Geophysical Research Letters*, *36*(2), L02102. https://doi.org/10.1029/2008GL036182

Davies, J. A., Perry, C. H., Trines, R. M. G. M., Harrison, R. A., Lugaz, N., Möstl, C., et al. (2013). Establishing a stereoscopic technique for determining the kinematic properties of solar wind transients based on a generalized self-similarly expanding circular geometry. *The Astrophysical Journal*, *777*, 167. https://doi.org/10.1088/0004-637X/777/2/167

Démoulin, P., Dasso, S., & Janvier, M. (2018). Exploring the biases of a new method based on minimum variance for interplanetary magnetic clouds. *Astronomy & Astrophysics*, *619*, A139. https://doi.org/10.1051/0004-6361/201833831

Démoulin, P., Priest, E. R., & Lonie, D. P. (1996). Three-dimensional magnetic reconnection without null points 2. Application to twisted flux tubes. *Journal of Geophysical Research*, *101*, 7631–7646. https://doi.org/10.1029/95JA03558

Desai, M., & Giacalone, J. (2016). Large gradual solar energetic particle events. *Living Reviews in Solar Physics*, *13*, 3. https://doi.org/10.1007/s41116-016-0002-5

Ding, L.-G., Jiang, Y., & Li, G. (2016). Are there two distinct solar energetic particle releases in the 2012 may 17 ground level enhancement event? *The Astrophysical Journal*, *818*(2), 169. https://doi.org/10.3847/0004-637X/818/2/169

Domingo, V., Fleck, B., & Poland, A. I. (1995). The SOHO mission: An overview. *Solar Physics*, *162*, 1–37. https://doi.org/10.1007/BF00733425

Dresing, N., Gómez-Herrero, R., Heber, B., Hidalgo, M. A., Klassen, A., Temmer, M., & Veronig, A. (2016). Injection of solar energetic particles into both loop legs of a magnetic cloud. *Astronomy & Astrophysics*, *586*, A55. https://doi.org/10.1051/0004-6361/201527347

Dresing, N., Gómez-Herrero, R., Heber, B., Klassen, A., Malandraki, O., Dröge, W., & Kartavykh, Y. (2014). Statistical survey of widely spread out solar electron events observed with STEREO and ACE with special attention to anisotropies. *Astronomy & Astrophysics*, *567*, A27. https://doi.org/10.1051/0004-6361/201423789

Dresing, N., Gómez-Herrero, R., Klassen, A., Heber, B., Kartavykh, Y., & Dröge, W. (2012). The large longitudinal spread of solar energetic particles during the 17 January 2010 solar event. *Solar Physics*, *281*(1), 281–300. https://doi.org/10.1007/s11207-012-0049-y

Eyles, C. J., Harrison, R. A., Davis, C. J., Waltham, N. R., Shaughnessy, B. M., Mapson-Menard, H. C. A., et al. (2009). The heliospheric imagers onboard the STEREO mission. *Solar Physics*, *254*, 387–445. https://doi.org/10.1007/s11207-008-9299-0

Fan, Y., & Gibson, S. E. (2004). Numerical simulations of three-dimensional coronal magnetic fields resulting from the emergence of twisted magnetic flux tubes. *The Astrophysical Journal*, *609*, 1123–1133. https://doi.org/10.1086/421238

Farrugia, C. J., Berdichevsky, D. B., Möstl, C., Galvin, A. B., Leitner, M., Popecki, M. A., et al. (2011). Multiple, distant (40°) in situ observations of a magnetic cloud and a corotating interaction region complex. *Journal of Atmospheric and Solar-Terrestrial Physics*, *73*(10), 1254–1269. https://doi.org/10.1016/j.jastp.2010.09.011

Farrugia, C. J., Janoo, L. A., Torbert, R. B., Quinn, J. M., Ogilvie, K. W., Lepping, R. P., et al. (1999). A uniform-twist magnetic flux rope in the solar wind. In S. R. Habbal, R. Esser, J. V. Hollweg, & P. A. Isenberg (Eds.), American institute of physics conference series (Vol. 471, pp. 745–748). American Institute of Physics. https://doi.org/10.1063/1.58724

Fazio, G. G., Hora, J. L., Allen, L. E., Ashby, M. L. N., Barmby, P., Deutsch, L. K., et al. (2004). The infrared Array camera (IRAC) for the spitzer space telescope. *The Astrophysical Journal - Supplement Series*, *154*(1), 10–17. https://doi.org/10.1086/422843

Forbes, T. G. (2000). A review on the genesis of coronal mass ejections. *Journal of Geophysical Research*, *105*, 23153–23166. https://doi.org/10.1029/2000JA000005

Forbush, S. E. (1937). On the effects in cosmic-ray intensity observed during the recent magnetic storm. *Physical Review*, *51*, 1108–1109. https://doi.org/10.1103/PhysRev.51.1108.3

Freiherr von Forstner, J. L., Guo, J., Wimmer-Schweingruber, R. F., Temmer, M., Dumbović, M., Veronig, A., et al. (2019). Tracking and validating ICMEs propagating toward Mars using STEREO heliospheric imagers combined with Forbush decreases detected by MSL/RAD. *Space Weather*, *17*(4), 586–598. https://doi.org/10.1029/2018SW002138

Futaana, Y., Barabash, S., Yamauchi, M., McKenna-Lawlor, S., Lundin, R., Luhmann, J. G., et al. (2008). Mars Express and Venus Express multi-point observations of geoeffective solar flare events in December 2006. *Planetary and Space Science*, *56*(6), 873–880. https://doi.org/10.1016/j.pss.2007.10.014

Gibson, S. E., & Fan, Y. (2006). Coronal prominence structure and dynamics: A magnetic flux rope interpretation. *Journal of Geophysical Research*, *111*(A12), A12103. https://doi.org/10.1029/2006JA011871

Gibson, S. E., Foster, D., Burkepile, J., de Toma, G., & Stanger, A. (2006). The calm before the storm: The link between quiescent cavities and coronal mass ejections. *The Astrophysical Journal*, *641*(1), 590–605. https://doi.org/10.1086/500446

Gold, T., & Hoyle, F. (1960). On the origin of solar flares. *Monthly Notices of the Royal Astronomical Society*, *120*, 89. https://doi.org/10.1093/mnras/120.2.89

Goldsten, J. O., Rhodes, E. A., Boynton, W. V., Feldman, W. C., Lawrence, D. J., Trombka, J. I., et al. (2007). The MESSENGER gamma-ray and neutron spectrometer. *Space Science Reviews*, *131*(1–4), 339–391. https://doi.org/10.1007/s11214-007-9262-7

Gopalswamy, N., Akiyama, S., Yashiro, S., & Xie, H. (2018). A new technique to provide realistic input to CME forecasting models. In C. Foullon, & O. E. Malandraki (Eds.), Space weather of the heliosphere: Processes and forecasts (Vol. 335, pp. 258–262). Cambridge University Press. https://doi.org/10.1017/S1743921317011048

Gopalswamy, N., Xie, H., Akiyama, S., Yashiro, S., Usoskin, I. G., & Davila, J. M. (2013). The first ground level enhancement event of solar cycle 24: Direct observation of shock formation and particle release heights. *The Astrophysical Journal Letters*, *765*(2), L30. https://doi.org/10.1088/2041-8205/765/2/L30

Green, L. M., Kliem, B., Török, T., van Driel-Gesztelyi, L., & Attrill, G. D. R. (2007). Transient coronal sigmoids and rotating erupting flux ropes. *Solar Physics*, *246*, 365–391. https://doi.org/10.1007/s11207-007-9061-z

Green, L. M., Török, T., Vršnak, B., Manchester, W., & Veronig, A. (2018). The origin, early evolution and predictability of solar eruptions. *Space Science Reviews*, *214*, 46. https://doi.org/10.1007/s11214-017-0462-5

Grotzinger, J. P., Crisp, J., Vasavada, A. R., Anderson, R. C., Baker, C. J., Barry, R., et al. (2012). Mars science laboratory mission and science investigation. *Space Science Reviews*, *170*(1–4), 5–56. https://doi.org/10.1007/s11214-012-9892-2

Guo, J., Dumbović, M., Wimmer-Schweingruber, R. F., Temmer, M., Lohf, H., Wang, Y., et al. (2018). Modeling the evolution and propagation of 10 September 2017 CMEs and SEPs arriving at Mars constrained by remote sensing and in situ measurement. *Space Weather*, *16*, 1156–1169. https://doi.org/10.1029/2018SW001973

Guo, J., Zeitlin, C., Wimmer-Schweingruber, R. F., Hassler, D. M., Posner, A., Heber, B., et al. (2015). Variations of dose rate observed by MSL/RAD in transit to Mars. *Astronomy & Astrophysics*, *577*, A58. https://doi.org/10.1051/0004-6361/201525680

Harrison, R. A., Davies, J. A., Barnes, D., Byrne, J. P., Perry, C. H., Bothmer, V., et al. (2018). CMEs in the heliosphere: I. A statistical analysis of the observational properties of CMEs detected in the heliosphere from 2007 to 2017 by STEREO/HI-1. *Solar Physics*, *293*(5), 77. https://doi.org/10.1007/s11207-018-1297-2

Hassler, D. M., Zeitlin, C., Ehresmann, B., Wimmer-Schweingruber, R. F., Guo, J., Matthiä, D., et al. (2018). Space weather on the surface of Mars: Impact of the September 2017 events. *Space Weather*, *16*(11), 1702–1708. https://doi.org/10.1029/2018SW001959

Hassler, D. M., Zeitlin, C., Wimmer-Schweingruber, R. F., Böttcher, S., Martin, C., Andrews, J., et al. (2012). The radiation assessment detector (RAD) investigation. *Space Science Reviews*, *170*, 503–558. https://doi.org/10.1007/s11214-012-9913-1

Heinemann, S. G., Temmer, M., Farrugia, C. J., Dissauer, K., Kay, C., Wiegelmann, T., et al. (2019). CME-HSS interaction and characteristics tracked from Sun to Earth. *Solar Physics*, *294*(9), 121. https://doi.org/10.1007/s11207-019-1515-6

Hess, V. F., & Demmelmair, A. (1937). World-wide effect in cosmic ray intensity, as observed during a recent magnetic storm. *Nature*, *140*, 316–317. https://doi.org/10.1038/140316a0

Howard, T. A., DeForest, C. E., Schneck, U. G., & Alden, C. R. (2017). Challenging some contemporary views of coronal mass ejections. II. The case for absent filaments. *The Astrophysical Journal*, *834*(1), 86. https://doi.org/10.3847/1538-4357/834/1/86

Howard, R. A., Moses, J. D., Vourlidas, A., Newmark, J. S., Socker, D. G., Plunkett, S. P., et al. (2008). Sun Earth connection coronal and heliospheric investigation (SECCHI). *Space Science Reviews*, *136*, 67–115. https://doi.org/10.1007/s11214-008-9341-4

Huttunen-Heikinmaa, K., Valtonen, E., & Laitinen, T. (2005). Proton and helium release times in SEP events observed with SOHO/ERNE. *Astronomy & Astrophysics*, *442*(2), 673–685. https://doi.org/10.1051/0004-6361:20042620

Isavnin, A., Vourlidas, A., & Kilpua, E. K. J. (2013). Three-dimensional evolution of erupted flux ropes from the Sun (2–20 $R_{\odot}$) to 1 AU. *Solar Physics*, *284*, 203–215. https://doi.org/10.1007/s11207-012-0214-3

Isavnin, A., Vourlidas, A., & Kilpua, E. K. J. (2014). Three-dimensional evolution of flux-rope CMEs and its relation to the local orientation of the heliospheric current sheet. *Solar Physics*, *289*, 2141–2156. https://doi.org/10.1007/s11207-013-0468-4

Jian, L. K., Russell, C. T., Luhmann, J. G., & Galvin, A. B. (2018). STEREO observations of interplanetary coronal mass ejections in 2007-2016. *The Astrophysical Journal*, *855*, 114. https://doi.org/10.3847/1538-4357/aab189

Kaiser, M. L., Kucera, T. A., Davila, J. M., St. Cyr, O. C., Guhathakurta, M., & Christian, E. (2008). The STEREO mission: An introduction. *Space Science Reviews*, *136*, 5–16. https://doi.org/10.1007/s11214-007-9277-0

Kay, C., & Opher, M. (2015). The heliocentric distance where the deflections and rotations of solar coronal mass ejections occur. *The Astrophysical Journal Letters*, *811*(2), L36. https://doi.org/10.1088/2041-8205/811/2/L36

Kay, C., Opher, M., & Evans, R. M. (2015). Global trends of CME deflections based on CME and solar parameters. *The Astrophysical Journal*, *805*, 168. https://doi.org/10.1088/0004-637X/805/2/168

Kilpua, E., Koskinen, H. E. J., & Pulkkinen, T. I. (2017). Coronal mass ejections and their sheath regions in interplanetary space. *Living Reviews in Solar Physics*, *14*, 5. https://doi.org/10.1007/s41116-017-0009-6

Kilpua, E. K. J., Good, S. W., Palmerio, E., Asvestari, E., Lumme, E., Ala-Lahti, M., et al. (2019). Multipoint observations of the June 2012 interacting interplanetary flux ropes. *Frontiers in Astronomy and Space Sciences*, *6*, 50. https://doi.org/10.3389/fspas.2019.00050

Kilpua, E. K. J., Lugaz, N., Mays, M. L., & Temmer, M. (2019). Forecasting the structure and orientation of Earthbound coronal mass ejections. *Space Weather*, *17*(4), 498–526. https://doi.org/10.1029/2018SW001944

Kilpua, E. K. J., Pomoell, J., Vourlidas, A., Vainio, R., Luhmann, J., Li, Y., et al. (2009). STEREO observations of interplanetary coronal mass ejections and prominence deflection during solar minimum period. *Annales Geophysicae*, *27*(12), 4491–4503. https://doi.org/10.5194/angeo-27-4491-2009

Klein, K.-L., & Dalla, S. (2017). Acceleration and propagation of solar energetic particles. *Space Science Reviews*, *212*, 1107–1136. https://doi.org/10.1007/s11214-017-0382-4

Kliem, B., Török, T., & Thompson, W. T. (2012). A parametric study of erupting flux rope rotation. Modeling the "Cartwheel CME" on 9 April 2008. *Solar Physics*, *281*(1), 137–166. https://doi.org/10.1007/s11207-012-9990-z

Koskinen, H. E. J., Baker, D. N., Balogh, A., Gombosi, T., Veronig, A., & von Steiger, R. (2017). Achievements and challenges in the science of space weather. *Space Science Reviews*, *212*(3–4), 1137–1157. https://doi.org/10.1007/s11214-017-0390-4

Kühl, P., Banjac, S., Dresing, N., Goméz-Herrero, R., Heber, B., Klassen, A., & Terasa, C. (2015). Proton intensity spectra during the solar energetic particle events of May 17, 2012 and January 6, 2014. *Astronomy & Astrophysics*, *576*, A120. https://doi.org/10.1051/0004-6361/201424874

Lario, D., & Karelitz, A. (2014). Influence of interplanetary coronal mass ejections on the peak intensity of solar energetic particle events. *Journal of Geophysical Research: Space Physics*, *119*(6), 4185–4209. https://doi.org/10.1002/2014JA019771

Lario, D., Kwon, R. Y., Richardson, I. G., Raouafi, N. E., Thompson, B. J., von Rosenvinge, T. T., et al. (2017). The solar energetic particle event of 2010 August 14: Connectivity with the solar source inferred from multiple spacecraft observations and modeling. *The Astrophysical Journal*, *838*(1), 51. https://doi.org/10.3847/1538-4357/aa63e4

Larson, D. E., Lin, R. P., McTiernan, J. M., McFadden, J. P., Ergun, R. E., McCarthy, M., et al. (1997). Tracing the topology of the October 18-20, 1995, magnetic cloud with ~0.1-10 keV electrons. *Geophysical Research Letters*, *24*(15), 1911–1914. https://doi.org/10.1029/97GL01878

Lee, C. O., Hara, T., Halekas, J. S., Thiemann, E., Chamberlin, P., Eparvier, F., et al. (2017). MAVEN observations of the solar cycle 24 space weather conditions at Mars. *Journal of Geophysical Research: Space Physics*, *122*(3), 2768–2794. https://doi.org/10.1002/2016JA023495

Lee, C. O., Jakosky, B. M., Luhmann, J. G., Brain, D. A., Mays, M. L., Hassler, D. M., et al. (2018). Observations and impacts of the 10 September 2017 solar events at Mars: An overview and synthesis of the initial results. *Geophysical Research Letters*, *45*, 8871–8885. https://doi.org/10.1029/2018GL079162

Lemen, J. R., Title, A. M., Akin, D. J., Boerner, P. F., Chou, C., Drake, J. F., et al. (2012). The atmospheric imaging assembly (AIA) on the solar dynamics observatory (SDO). *Solar Physics*, *275*, 17–40. https://doi.org/10.1007/s11207-011-9776-8

Lepping, R. P., Acũna, M. H., Burlaga, L. F., Farrell, W. M., Slavin, J. A., Schatten, K. H., et al. (1995). The wind magnetic field investigation. *Space Science Reviews*, *71*, 207–229. https://doi.org/10.1007/BF00751330

Lepping, R. P., Berdichevsky, D. B., & Ferguson, T. J. (2003). Estimated errors in magnetic cloud model fit parameters with force-free cylindrically symmetric assumptions. *Journal of Geophysical Research*, *108*(A10), 1356. https://doi.org/10.1029/2002JA009657

Lepping, R. P., Burlaga, L. F., & Jones, J. A. (1990). Magnetic field structure of interplanetary magnetic clouds at 1 AU. *Journal of Geophysical Research*, *95*, 11957–11965. https://doi.org/10.1029/JA095iA08p11957

Li, C., Firoz, K. A., Sun, L. P., & Miroshnichenko, L. I. (2013). Electron and proton acceleration during the first ground level enhancement event of solar cycle 24. *The Astrophysical Journal*, *770*(1), 34. https://doi.org/10.1088/0004-637X/770/1/34

Liu, R., Alexander, D., & Gilbert, H. R. (2009). Asymmetric eruptive filaments. *The Astrophysical Journal*, *691*(2), 1079–1091. https://doi.org/10.1088/0004-637X/691/2/1079

Liu, Y., Shen, F., & Yang, Y. (2019). Numerical simulation on the propagation and deflection of fast coronal mass ejections (CMEs) interacting with a corotating interaction region in interplanetary space. *The Astrophysical Journal*, *887*(2), 150. https://doi.org/10.3847/1538-4357/ab543e

Lowrance, P. J., Krick, J. E., Ingalls, J. G., Laine, S., Carey, S. J., Glaccum, W., et al. (2018). Calibration trending in the Spitzer beyond era. In: A. B. Peck R. L. Seaman & C. R. Benn Observatory operations: Strategies, processes, and systems vii (Vol. 10704, p. 1070427). SPIE Press. https://doi.org/10.1117/12.2313953

Lucas, J. M. (1985). Counted data CUSUM's. *Technometrics*, *27*(2), 129–144. https://doi.org/10.1080/00401706.1985.10488030

Lugaz, N., Downs, C., Shibata, K., Roussev, I. I., Asai, A., & Gombosi, T. I. (2011). Numerical investigation of a coronal mass ejection from an anemone active region: Reconnection and deflection of the 2005 August 22 eruption. *The Astrophysical Journal*, *738*(2), 127. https://doi.org/10.1088/0004-637X/738/2/127

Lugaz, N., & Farrugia, C. J. (2014). A new class of complex ejecta resulting from the interaction of two CMEs and its expected geoeffectiveness. *Geophysical Research Letters*, *41*(3), 769–776. https://doi.org/10.1002/2013GL058789

Lugaz, N., Farrugia, C. J., Manchester, I. W. B., & Schwadron, N. (2013). The interaction of two coronal mass ejections: Influence of relative orientation. *The Astrophysical Journal*, *778*(1), 20. https://doi.org/10.1088/0004-637X/778/1/20

Lugaz, N., Temmer, M., Wang, Y., & Farrugia, C. J. (2017). The interaction of successive coronal mass ejections: A review. *Solar Physics*, *292*(4), 64. https://doi.org/10.1007/s11207-017-1091-6

Luhmann, J. G., Curtis, D. W., Schroeder, P., McCauley, J., Lin, R. P., Larson, D. E., et al. (2008). STEREO IMPACT investigation goals, measurements, and data products overview. *Space Science Reviews*, *136*, 117–184. https://doi.org/10.1007/s11214-007-9170-x

Luhmann, J. G., Dong, C. F., Ma, Y. J., Curry, S. M., Xu, S., Lee, C. O., et al. (2017). Martian magnetic storms. *Journal of Geophysical Research: Space Physics*, *122*(6), 6185–6209. https://doi.org/10.1002/2016JA023513

Luhmann, J. G., Gopalswamy, N., Jian, L. K., & Lugaz, N. (2020). ICME evolution in the inner heliosphere. *Solar Physics*, *295*(4), 61. https://doi.org/10.1007/s11207-020-01624-0

Lundquist, S. (1950). Magnetohydrostatic fields. *Arkiv för Fysik*, *2*, 361–365.

Lynch, B. J., Antiochos, S. K., Li, Y., Luhmann, J. G., & DeVore, C. R. (2009). Rotation of coronal mass ejections during eruption. *The Astrophysical Journal*, *697*, 1918–1927. https://doi.org/10.1088/0004-637X/697/2/1918

Lynch, B. J., & Edmondson, J. K. (2013). Sympathetic magnetic breakout coronal mass ejections from pseudostreamers. *The Astrophysical Journal*, *764*, 87. https://doi.org/10.1088/0004-637X/764/1/87

Malandraki, O. E., & Crosby, N. B. (2018). Solar energetic particles and space weather: Science and applications. In O. E. Malandraki, & N. B. Crosby (Eds.), Solar particle radiation storms forecasting and analysis (Vol. 444, pp. 1–26). Springer. https://doi.org/10.1007/978-3-319-60051-2_1

Manchester, W., Kilpua, E. K. J., Liu, Y. D., Lugaz, N., Riley, P., Török, T., & Vršnak, B. (2017). The physical processes of CME/ICME evolution. *Space Science Reviews*, *212*(3–4). https://doi.org/10.1007/s11214-017-0394-0

Manchester, W. B., Gombosi, T. I., Roussev, I., Ridley, A., de Zeeuw, D. L., Sokolov, I. V., et al. (2004). Modeling a space weather event from the Sun to the Earth: CME generation and interplanetary propagation. *Journal of Geophysical Research*, *109*(A2), A02107. https://doi.org/10.1029/2003JA010150

Martin, S. F., Panasenco, O., Berger, M. A., Engvold, O., Lin, Y., Pevtsov, A. A., & Srivastava, N. (2012). The build-up to eruptive solar events viewed as the development of chiral systems. In T. R. Rimmele, et al. (Eds.), Second ATST-EAST meeting: Magnetic fields from the photosphere to the corona (463, pp. 157).Astronomical Society of the Pacific.

Masson, S., Démoulin, P., Dasso, S., & Klein, K. L. (2012). The interplanetary magnetic structure that guides solar relativistic particles. *Astronomy & Astrophysics*, *538*, A32. https://doi.org/10.1051/0004-6361/201118145

Mays, M. L., Taktakishvili, A., Pulkkinen, A., MacNeice, P. J., Rastätter, L., Odstrcil, D., et al. (2015). Ensemble modeling of CMEs using the WSA-ENLIL+Cone model. *Solar Physics*, *290*(6), 1775–1814. https://doi.org/10.1007/s11207-015-0692-1

Morgan, D. D., Diéval, C., Gurnett, D. A., Duru, F., Dubinin, E. M., Fränz, M., et al. (2014). Effects of a strong ICME on the Martian ionosphere as detected by Mars Express and Mars Odyssey. *Journal of Geophysical Research: Space Physics*, *119*(7), 5891–5908. https://doi.org/10.1002/2013JA019522

Möstl, C., Amerstorfer, T., Palmerio, E., Isavnin, A., Farrugia, C. J., Lowder, C., et al. (2018). Forward modeling of coronal mass ejection flux ropes in the inner heliosphere with 3DCORE. *Space Weather*, *16*, 216–229. https://doi.org/10.1002/2017SW001735

Möstl, C., & Davies, J. A. (2013). Speeds and arrival times of solar transients approximated by self-similar expanding circular fronts. *Solar Physics*, *285*, 411–423. https://doi.org/10.1007/s11207-012-9978-8

Möstl, C., Farrugia, C. J., Kilpua, E. K. J., Jian, L. K., Liu, Y., Eastwood, J. P., et al. (2012). Multi-point shock and flux rope analysis of multiple interplanetary coronal mass ejections around 2010 August 1 in the inner heliosphere. *The Astrophysical Journal*, *758*, 10. https://doi.org/10.1088/0004-637X/758/1/10

Möstl, C., Isavnin, A., Boakes, P. D., Kilpua, E. K. J., Davies, J. A., Harrison, R. A., et al. (2017). Modeling observations of solar coronal mass ejections with heliospheric imagers verified with the Heliophysics System Observatory. *Space Weather*, *15*, 955–970. https://doi.org/10.1002/2017SW001614

Möstl, C., Rollett, T., Frahm, R. A., Liu, Y. D., Long, D. M., Colaninno, R. C., et al. (2015). Strong coronal channelling and interplanetary evolution of a solar storm up to Earth and Mars. *Nature Communications*, *6*, 7135. https://doi.org/10.1038/ncomms8135

Müller, D., Nicula, B., Felix, S., Verstringe, F., Bourgoignie, B., Csillaghy, A., et al. (2017). JHelioviewer. Time-dependent 3D visualisation of solar and heliospheric data. *Astronomy & Astrophysics*, *606*, A10. https://doi.org/10.1051/0004-6361/201730893

Mulligan, T., Russell, C. T., & Luhmann, J. G. (1998). Solar cycle evolution of the structure of magnetic clouds in the inner heliosphere. *Geophysical Research Letters*, *25*, 2959–2962. https://doi.org/10.1029/98GL01302

Nieves-Chinchilla, T., Colaninno, R., Vourlidas, A., Szabo, A., Lepping, R. P., Boardsen, S. A., et al. (2012). Remote and in situ observations of an unusual Earth-directed coronal mass ejection from multiple viewpoints. *Journal of Geophysical Research*, *117*(A6), A06106. https://doi.org/10.1029/2011JA017243

Nieves-Chinchilla, T., Jian, L. K., Balmaceda, L., Vourlidas, A., dos Santos, L. F. G., & Szabo, A. (2019). Unraveling the internal magnetic field structure of the Earth-directed interplanetary coronal mass ejections during 1995 - 2015. *Solar Physics*, *294*(7), 89. https://doi.org/10.1007/s11207-019-1477-8

Nieves-Chinchilla, T., Linton, M. G., Hidalgo, M. A., Vourlidas, A., Savani, N. P., Szabo, A., et al. (2016). A circular-cylindrical flux-rope analytical model for magnetic clouds. *The Astrophysical Journal*, *823*(1), 27. https://doi.org/10.3847/0004-637X/823/1/27

Nieves-Chinchilla, T., Szabo, A., Korreck, K. E., Alzate, N., Balmaceda, L. A., Lavraud, B., et al. (2020). Analysis of the internal structure of the streamer blowout observed by the Parker solar probe during the first solar encounter. *The Astrophysical Journal-Supplement Series*, *246*(2), 63. https://doi.org/10.3847/1538-4365/ab61f5

Nieves-Chinchilla, T., Vourlidas, A., Raymond, J. C., Linton, M. G., Al-haddad, N., Savani, N. P., et al. (2018). Understanding the internal magnetic field configurations of ICMEs using more than 20 Years of wind observations. *Solar Physics*, *293*, 25. https://doi.org/10.1007/s11207-018-1247-z

Nitta, N. V., Liu, Y., DeRosa, M. L., & Nightingale, R. W. (2012). What are special about ground-level events? Flares, CMEs, active regions and magnetic field connection. *Space Science Reviews*, *171*(1–4), 61–83. https://doi.org/10.1007/s11214-012-9877-1

Odstrcil, D. (2003). Modeling 3-D solar wind structure. *Advances in Space Research*, *32*, 497–506. https://doi.org/10.1016/S0273-1177(03)00332-6

Odstrcil, D., Riley, P., & Zhao, X. P. (2004). Numerical simulation of the 12 May 1997 interplanetary CME event. *Journal of Geophysical Research*, *109*(A2), A02116. https://doi.org/10.1029/2003JA010135

Ogilvie, K. W., Chornay, D. J., Fritzenreiter, R. J., Hunsaker, F., Keller, J., Lobell, J., et al. (1995). SWE, a comprehensive plasma instrument for the wind spacecraft. *Space Science Reviews*, *71*, 55–77. https://doi.org/10.1007/BF00751326

Owens, M. J. (2008). Combining remote and in situ observations of coronal mass ejections to better constrain magnetic cloud reconstruction. *Journal of Geophysical Research*, *113*(A12), A12102. https://doi.org/10.1029/2008JA013589

Owens, M. J., & Forsyth, R. J. (2013). The heliospheric magnetic field. *Living Reviews in Solar Physics*, *10*(1), 5. https://doi.org/10.12942/lrsp-2013-5

Owens, M. J., Lockwood, M., & Barnard, L. A. (2017). Coronal mass ejections are not coherent magnetohydrodynamic structures. *Scientific Reports*, *7*, 4152. https://doi.org/10.1038/s41598-017-04546-3

Palmerio, E., Kilpua, E. K. J., James, A. W., Green, L. M., Pomoell, J., Isavnin, A., & Valori, G. (2017). Determining the intrinsic CME flux rope type using remote-sensing solar disk observations. *Solar Physics*, *292*(2), 39. https://doi.org/10.1007/s11207-017-1063-x

Palmerio, E., Kilpua, E. K. J., Möstl, C., Bothmer, V., James, A. W., Green, L. M., et al. (2018). Coronal magnetic structure of Earthbound CMEs and in situ comparison. *Space Weather*, *16*(5), 442–460. https://doi.org/10.1002/2017SW001767

Palmerio, E., Scolini, C., Barnes, D., Magdalenić, J., West, M. J., Zhukov, A. N., et al. (2019). Multipoint study of successive coronal mass ejections driving moderate disturbances at 1 AU. *The Astrophysical Journal*, *878*(1), 37. https://doi.org/10.3847/1538-4357/ab1850

Parker, E. N. (1958). Dynamics of the interplanetary gas and magnetic fields. *The Astrophysical Journal*, *128*, 664. https://doi.org/10.1086/146579

Pesnell, W. D., Thompson, B. J., & Chamberlin, P. C. (2012). The solar dynamics observatory (SDO). *Solar Physics*, *275*, 3–15. https://doi.org/10.1007/s11207-011-9841-3

Picardi, G., Biccari, D., Seu, R., Plaut, J., Johnson, W. T. K., Jordan, R. L., et al. (2004). MARSIS: Mars advanced radar for subsurface and ionosphere sounding. In A. Wilson, & A. Chicarro (Eds.), Mars express: The scientific payload. (Vol. 1240, pp. 51–69). European Space Agency Special Publication.

Plainaki, C., Mavromichalaki, H., Laurenza, M., Gerontidou, M., Kanellakopoulos, A., & Storini, M. (2014). The ground-level enhancement of 2012 may 17: Derivation of solar proton event properties through the application of the NMBANGLE PPOLA model. *The Astrophysical Journal*, *785*(2), 160. https://doi.org/10.1088/0004-637X/785/2/160

Prise, A. J., Harra, L. K., Matthews, S. A., Arridge, C. S., & Achilleos, N. (2015). Analysis of a coronal mass ejection and corotating interaction region as they travel from the Sun passing Venus, Earth, Mars, and Saturn. *Journal of Geophysical Research: Space Physics*, *120*, 1566–1588. https://doi.org/10.1002/2014JA020256

Ramstad, R., Holmström, M., Futaana, Y., Lee, C. O., Rahmati, A., Dunn, P., et al. (2018). The september 2017 SEP event in context with the current solar cycle: Mars express ASPERA-3/IMA and MAVEN/SEP observations. *Geophysical Research Letters*, *45*(15), 7306–7311. https://doi.org/10.1029/2018GL077842

Reames, D. V. (1990). Energetic particles from impulsive solar flares. *The Astrophysical Journal-Supplement Series*, *73*, 235. https://doi.org/10.1086/191456

Reames, D. V. (1999). Particle acceleration at the Sun and in the heliosphere. *Space Science Reviews*, *90*, 413–491. https://doi.org/10.1023/A:1005105831781

Reames, D. V. (2002). Magnetic topology of impulsive and gradual solar energetic particle events. *The Astrophysical Journal Letters*, *571*(1), L63–L66. https://doi.org/10.1086/341149

Reames, D. V. (2013). The two sources of solar energetic particles. *Space Science Reviews*, *175*(1–4), 53–92. https://doi.org/10.1007/s11214-013-9958-9

Reames, D. V. (2015). What are the sources of solar energetic particles? Element abundances and source plasma temperatures. *Space Science Reviews*, *194*(1–4), 303–327. https://doi.org/10.1007/s11214-015-0210-7

Richardson, I. G., & Cane, H. V. (1995). Regions of abnormally low proton temperature in the solar wind (1965-1991) and their association with ejecta. *Journal of Geophysical Research*, *100*(A12), 23397–23412. https://doi.org/10.1029/95JA02684

Richardson, I. G., & Cane, H. V. (2010). Near-earth interplanetary coronal mass ejections during solar cycle 23 (1996–2009): Catalog and summary of properties. *Solar Physics*, *264*, 189–237. https://doi.org/10.1007/s11207-010-9568-6

Richardson, I. G., von Rosenvinge, T. T., Cane, H. V., Christian, E. R., Cohen, C. M. S., Labrador, A. W., et al. (2014). >25 MeV proton events observed by the high energy telescopes on the STEREO A and B spacecraft and/or at Earth during the first ~ seven years of the STEREO mission. *Solar Physics*, *289*(8), 3059–3107. https://doi.org/10.1007/s11207-014-0524-8

Riley, P., Linker, J. A., Lionello, R., Mikić, Z., Odstrcil, D., Hidalgo, M. A., et al. (2004). Fitting flux ropes to a global MHD solution: A comparison of techniques. *Journal of Atmospheric and Solar-Terrestrial Physics*, *66*(15–16), 1321–1331. https://doi.org/10.1016/j.jastp.2004.03.019

Riley, P., Mays, M. L., Andries, J., Amerstorfer, T., Biesecker, D., Delouille, V., et al. (2018). Forecasting the arrival time of coronal mass ejections: Analysis of the CCMC CME scoreboard. *Space Weather*, *16*, 1245–1260. https://doi.org/10.1029/2018SW001962

Rodriguez, L., Krupp, N., Woch, J., & Fränz, M. (2008). Elemental abundances of energetic particles within magnetic clouds detected by Ulysses. *The Astrophysical Journal*, *673*(1), 621–628. https://doi.org/10.1086/523999

Rodriguez, L., Masías-Meza, J. J., Dasso, S., Démoulin, P., Zhukov, A. N., Gulisano, A. M., et al. (2016). Typical profiles and distributions of plasma and magnetic field parameters in magnetic clouds at 1 AU. *Solar Physics*, *291*, 2145–2163. https://doi.org/10.1007/s11207-016-0955-5

Rodriguez, L., Mierla, M., Zhukov, A. N., West, M., & Kilpua, E. (2011). Linking remote-sensing and in situ observations of coronal mass ejections using STEREO. *Solar Physics*, *270*(2), 561–573. https://doi.org/10.1007/s11207-011-9784-8

Rouillard, A. P., Lavraud, B., Sheeley, N. R., Davies, J. A., Burlaga, L. F., Savani, N. P., et al. (2010). White light and in situ comparison of a forming merged interaction region. *The Astrophysical Journal*, *719*(2), 1385–1392. https://doi.org/10.1088/0004-637X/719/2/1385

Rouillard, A. P., Plotnikov, I., Pinto, R. F., Tirole, M., Lavarra, M., Zucca, P., et al. (2016). Deriving the properties of coronal pressure fronts in 3D: Application to the 2012 may 17 ground level enhancement. *The Astrophysical Journal*, *833*, 45. https://doi.org/10.3847/1538-4357/833/1/45

Rouillard, A. P., Sheeley, N. R., Tylka, A., Vourlidas, A., Ng, C. K., Rakowski, C., et al. (2012). The longitudinal properties of a solar energetic particle event investigated using modern solar imaging. *The Astrophysical Journal*, *752*(1), 44. https://doi.org/10.1088/0004-637X/752/1/44

Sánchez-Cano, B., Hall, B. E. S., Lester, M., Mays, M. L., Witasse, O., Ambrosi, R., et al. (2017). Mars plasma system response to solar wind disturbances during solar minimum. *Journal of Geophysical Research: Space Physics*, *122*(6), 6611–6634. https://doi.org/10.1002/2016JA023587

Sánchez-Cano, B., Narvaez, C., Lester, M., Mendillo, M., Mayyasi, M., Holmstrom, M., et al. (2020). Mars' ionopause: A matter of pressures. *Journal of Geophysical Research: Space Physics*, *125*(9), e2020JA028145. https://doi.org/10.1029/2020JA028145

Sánchez-Cano, B., Witasse, O., Lester, M., Rahmati, A., Ambrosi, R., Lillis, R., et al. (2018). Energetic particle showers over Mars from comet C/2013 A1 siding spring. *Journal of Geophysical Research: Space Physics*, *123*(10), 8778–8796. https://doi.org/10.1029/2018JA025454

Saunders, R. S., Arvidson, R. E., Badhwar, G. D., Boynton, W. V., Christensen, P. R., Cucinotta, F. A., et al. (2004). 2001 Mars Odyssey mission summary. *Space Science Reviews*, *110*(1), 1–36. https://doi.org/10.1023/B:SPAC.0000021006.84299.18

Savani, N. P., Owens, M. J., Rouillard, A. P., Forsyth, R. J., & Davies, J. A. (2010). Observational evidence of a coronal mass ejection distortion directly attributable to a structured solar wind. *The Astrophysical Journal Letters*, *714*, L128–L132. https://doi.org/10.1088/2041-8205/714/1/L128

Savani, N. P., Vourlidas, A., Szabo, A., Mays, M. L., Richardson, I. G., Thompson, B. J., et al. (2015). Predicting the magnetic vectors within coronal mass ejections arriving at Earth: 1. Initial architecture. *Space Weather*, *13*, 374–385. https://doi.org/10.1002/2015SW001171

Scherrer, P. H., Schou, J., Bush, R. I., Kosovichev, A. G., Bogart, R. S., Hoeksema, J. T., et al. (2012). The helioseismic and magnetic imager (HMI) investigation for the solar dynamics observatory (SDO). *Solar Physics*, *275*, 207–227. https://doi.org/10.1007/s11207-011-9834-2

Schmieder, B., van Driel-Gesztelyi, L., Aulanier, G., Démoulin, P., Thompson, B., De Forest, C., et al. (2002). Relationships between CME's and prominences. *Advances in Space Research*, *29*(10), 1451–1460. https://doi.org/10.1016/S0273-1177(02)00211-9

Scolini, C., Chané, E., Temmer, M., Kilpua, E. K. J., Dissauer, K., Veronig, A. M., et al. (2020). CME–CME interactions as sources of CME geoeffectiveness: The formation of the complex ejecta and intense geomagnetic storm in 2017 early september. *The Astrophysical Journal-Supplement Series*, *247*(1), 21. https://doi.org/10.3847/1538-4365/ab6216

Sheeley, N. R., Jr., Herbst, A. D., Palatchi, C. A., Wang, Y.-M., Howard, R. A., Moses, J. D., et al. (2008). Heliospheric images of the solar wind at Earth. *The Astrophysical Journal*, *675*, 853–862. https://doi.org/10.1086/526422

Shen, C., Li, G., Kong, X., Hu, J., Sun, X. D., Ding, L., et al. (2013). Compound twin coronal mass ejections in the 2012 may 17 GLE event. *The Astrophysical Journal*, *763*(2), 114. https://doi.org/10.1088/0004-637X/763/2/114

Solomon, S. C., McNutt, R. L., Gold, R. E., & Domingue, D. L. (2007). MESSENGER mission overview. *Space Science Reviews*, *131*, 3–39. https://doi.org/10.1007/s11214-007-9247-6

Sonnerup, B. U. O., & Cahill, L. J., Jr. (1967). Magnetopause structure and attitude from explorer 12 observations. *Journal of Geophysical Research*, *72*, 171. https://doi.org/10.1029/JZ072i001p00171
SunPy Community, Barnes, W. T., Bobra, M. G., Christe, S. D., Freij, N., Hayes, L. A., et al. (2020). The SunPy project: Open source development and status of the version 1.0 core package. *The Astrophysical Journal*, *890*(1), 68. https://doi.org/10.3847/1538-4357/ab4f7a
SunPy Community, Mumford, S. J., Christe, S., Pérez-Suárez, D., Ireland, J., Shih, A. Y., et al. (2015). SunPy—Python for solar physics. *Computational Science & Discovery*, *8*(1), 014009. https://doi.org/10.1088/1749-4699/8/1/014009
Svedhem, H., Titov, D. V., McCoy, D., Lebreton, J. P., Barabash, S., Bertaux, J. L., et al. (2007). Venus express—The first European mission to Venus. *Planetary and Space Science*, *55*, 1636–1652. https://doi.org/10.1016/j.pss.2007.01.013
Thernisien, A. (2011). Implementation of the graduated cylindrical shell model for the three-dimensional reconstruction of coronal mass ejections. *The Astrophysical Journal-Supplement Series*, *194*, 33. https://doi.org/10.1088/0067-0049/194/2/33
Thernisien, A., Vourlidas, A., & Howard, R. A. (2009). Forward modeling of coronal mass ejections using STEREO/SECCHI data. *Solar Physics*, *256*, 111–130. https://doi.org/10.1007/s11207-009-9346-5
Thernisien, A. F. R., Howard, R. A., & Vourlidas, A. (2006). Modeling of flux rope coronal mass ejections. *The Astrophysical Journal*, *652*, 763–773. https://doi.org/10.1086/508254
Thompson, W. T. (2006). Coordinate systems for solar image data. *Astronomy & Astrophysics*, *449*(2), 791–803. https://doi.org/10.1051/0004-6361:20054262
Thompson, W. T. (2009). 3D triangulation of a Sun-grazing comet. *Icarus*, *200*, 351–357. https://doi.org/10.1016/j.icarus.2008.12.011
Thompson, B. J., Cliver, E. W., Nitta, N., Delannée, C., & Delaboudinière, J.-P. (2000). Coronal dimmings and energetic CMEs in April-May 1998. *Geophysical Research Letters*, *27*, 1431–1434. https://doi.org/10.1029/1999GL003668
Thompson, B. J., Plunkett, S. P., Gurman, J. B., Newmark, J. S., St. Cyr, O. C., & Michels, D. J. (1998). SOHO/EIT observations of an Earth-directed coronal mass ejection on May 12, 1997. *Geophysical Research Letters*, *25*, 2465–2468. https://doi.org/10.1029/98GL50429
Thompson, W. T., Kliem, B., & Török, T. (2012). 3D reconstruction of a rotating erupting prominence. *Solar Physics*, *276*, 241–259. https://doi.org/10.1007/s11207-011-9868-5
Török, T., Panasenco, O., Titov, V. S., Mikić, Z., Reeves, K. K., Velli, M., et al. (2011). A model for magnetically coupled sympathetic eruptions. *The Astrophysical Journal Letters*, *739*(2), L63. https://doi.org/10.1088/2041-8205/739/2/L63
Tripathi, D., Isobe, H., & Mason, H. E. (2006). On the propagation of brightening after filament/prominence eruptions, as seen by SoHO-EIT. *Astronomy & Astrophysics*, *453*(3), 1111–1116. https://doi.org/10.1051/0004-6361:20064993
Vainio, R., Desorgher, L., Heynderickx, D., Storini, M., Flückiger, E., Horne, R. B., et al. (2009). Dynamics of the Earth's particle radiation environment. *Space Science Reviews*, *147*(3–4), 187–231. https://doi.org/10.1007/s11214-009-9496-7
Vandas, M., & Romashets, E. (2017). Magnetic cloud fit by uniform-twist toroidal flux ropes. *Astronomy & Astrophysics*, *608*, A118. https://doi.org/10.1051/0004-6361/201731412
Velli, M., Harra, L. K., Vourlidas, A., Schwadron, N., Panasenco, O., Liewer, P. C., et al. (2020). Understanding the origins of the heliosphere: Integrating observations and measurements from Parker solar probe, solar orbiter, and other space- and ground-based observatories. *Astronomy & Astrophysics*, *642*, A4. https://doi.org/10.1051/0004-6361/202038245
Verbeke, C., Mays, M. L., Temmer, M., Bingham, S., Steenburgh, R., Dumbović, M., et al. (2019). Benchmarking CME arrival time and impact: Progress on metadata, metrics, and events. *Space Weather*, *17*(1), 6–26. https://doi.org/10.1029/2018SW002046
Vlahos, L., Anastasiadis, A., Papaioannou, A., Kouloumvakos, A., & Isliker, H. (2019). Sources of solar energetic particles. *Philosophical Transactions of the Royal Society of London, Series A*, *377*(2148), 20180095. https://doi.org/10.1098/rsta.2018.0095
von Rosenvinge, T. T., Reames, D. V., Baker, R., Hawk, J., Nolan, J. T., Ryan, L., et al. (2008). The high energy telescope for STEREO. *Space Science Reviews*, *136*(1–4), 391–435. https://doi.org/10.1007/s11214-007-9300-5
Vourlidas, A., Balmaceda, L. A., Stenborg, G., & Dal Lago, A. (2017). Multi-viewpoint coronal mass ejection catalog based on STEREO COR2 observations. *The Astrophysical Journal*, *838*, 141. https://doi.org/10.3847/1538-4357/aa67f0
Vourlidas, A., Colaninno, R., Nieves-Chinchilla, T., & Stenborg, G. (2011). The first observation of a rapidly rotating coronal mass ejection in the middle corona. *The Astrophysical Journal Letters*, *733*, L23. https://doi.org/10.1088/2041-8205/733/2/L23
Vourlidas, A., Lynch, B. J., Howard, R. A., & Li, Y. (2013). How many CMEs have flux ropes? Deciphering the signatures of shocks, flux ropes, and prominences in coronagraph observations of CMEs. *Solar Physics*, *284*, 179–201. https://doi.org/10.1007/s11207-012-0084-8
Vourlidas, A., Patsourakos, S., & Savani, N. P. (2019). Predicting the geoeffective properties of coronal mass ejections: Current status, open issues and path forward. *Philosophical Transactions of the Royal Society of London, Series A*, *377*(2148), 20180096. https://doi.org/10.1098/rsta.2018.0096
Vršnak, B., Žic, T., Vrbanec, D., Temmer, M., Rollett, T., Möstl, C., et al. (2013). Propagation of interplanetary coronal mass ejections: The drag-based model. *Solar Physics*, *285*, 295–315. https://doi.org/10.1007/s11207-012-0035-4
Wang, Y., Shen, C., Wang, S., & Ye, P. (2004). Deflection of coronal mass ejection in the interplanetary medium. *Solar Physics*, *222*(2), 329–343. https://doi.org/10.1023/B:SOLA.0000043576.21942.aa
Webb, D. F., & Howard, T. A. (2012). Coronal mass ejections: Observations. *Living Reviews in Solar Physics*, *9*(1), 3. https://doi.org/10.12942/lrsp-2012-3
Weiss, A. J., Möstl, C., Amerstorfer, T., Bailey, R. L., Reiss, M. A., Hinterreiter, J., et al. (2021). Analysis of coronal mass ejection flux rope signatures using 3DCORE and approximate Bayesian Computation. *The Astrophysical Journal Supplement Series*. *252*(9). https://doi.org/10.3847/1538-4365/abc9bd
Werner, M. W., Roellig, T. L., Low, F. J., Rieke, G. H., Rieke, M., Hoffmann, W. F., et al. (2004). The spitzer space telescope mission. *The Astrophysical Journal-Supplement Series*, *154*(1), 1–9. https://doi.org/10.1086/422992
Wibberenz, G., & Cane, H. V. (2006). Multi-Spacecraft observations of solar flare particles in the inner heliosphere. *The Astrophysical Journal*, *650*(2), 1199–1207. https://doi.org/10.1086/506598
Wiedenbeck, M. E., Mason, G. M., Cohen, C. M. S., Nitta, N. V., Gómez-Herrero, R., & Haggerty, D. K. (2013). Observations of solar energetic particles from 3He-rich events over a wide range of heliographic longitude. *The Astrophysical Journal*, *762*(1), 54. https://doi.org/10.1088/0004-637X/762/1/54
Winslow, R. M., Lugaz, N., Philpott, L. C., Schwadron, N. A., Farrugia, C. J., Anderson, B. J., & Smith, C. W. (2015). Interplanetary coronal mass ejections from MESSENGER orbital observations at Mercury. *Journal of Geophysical Research: Space Physics*, *120*(8), 6101–6118. https://doi.org/10.1002/2015JA021200
Winslow, R. M., Lugaz, N., Schwadron, N. A., Farrugia, C. J., Yu, W., Raines, J. M., et al. (2016). Longitudinal conjunction between MESSENGER and STEREO A: Development of ICME complexity through stream interactions. *Journal of Geophysical Research: Space Physics*, *121*(7), 6092–6106. https://doi.org/10.1002/2015JA022307

Witasse, O., Sánchez-Cano, B., Mays, M. L., Kajdič, P., Opgenoorth, H., Elliott, H. A., et al. (2017). Interplanetary coronal mass ejection observed at STEREO-A, Mars, comet 67P/Churyumov-Gerasimenko, Saturn, and New Horizons en route to Pluto: Comparison of its Forbush decreases at 1.4, 3.1, and 9.9 AU. *Journal of Geophysical Research: Space Physics*, *122*, 7865–7890. https://doi.org/10.1002/2017JA023884

Wold, A. M., Mays, M. L., Taktakishvili, A. r., Jian, L. K., Odstrcil, D., & MacNeice, P. (2018). Verification of real-time WSA-ENLIL+Cone simulations of CME arrival-time at the CCMC from 2010 to 2016. *Journal of Space Weather and Space Climate*, *8*, A17. https://doi.org/10.1051/swsc/2018005

Xie, H., St. Cyr, O. C., Gopalswamy, N., Yashiro, S., Krall, J., Kramar, M., & Davila, J. (2009). On the origin, 3D structure and dynamic evolution of CMEs near solar minimum. *Solar Physics*, *259*(1–2), 143–161. https://doi.org/10.1007/s11207-009-9422-x

Xu, Z., Guo, J., Wimmer-Schweingruber, R. F., Freiherr von Forstner, J. L., Wang, Y., Dresing, N., et al. (2020). First solar energetic particles measured on the lunar far-side. *The Astrophysical Journal Letters*, *902*(2), L30. https://doi.org/10.3847/2041-8213/abbccc

Yurchyshyn, V. (2008). Relationship between EIT posteruption arcades, coronal mass ejections, the coronal neutral line, and magnetic clouds. *The Astrophysical Journal Letters*, *675*(1), L49. https://doi.org/10.1086/533413

Zeitlin, C., Hassler, D. M., Cucinotta, F. A., Ehresmann, B., Wimmer-Schweingruber, R. F., Brinza, D. E., et al. (2013). Measurements of energetic particle radiation in transit to Mars on the Mars science laboratory. *Science*, *340*(6136), 1080–1084. https://doi.org/10.1126/science.1235989

Zeitlin, C., Hassler, D. M., Guo, J., Ehresmann, B., Wimmer-Schweingruber, R. F., Rafkin, S. C. R., et al. (2018). Analysis of the radiation hazard observed by RAD on the surface of Mars during the september 2017 solar particle event. *Geophysical Research Letters*, *45*(12), 5845–5851. https://doi.org/10.1029/2018GL077760

Zhang, T. L., Baumjohann, W., Delva, M., Auster, H.-U., Balogh, A., Russell, C. T., et al. (2006). Magnetic field investigation of the Venus plasma environment: Expected new results from Venus Express. *Planetary and Space Science*, *54*, 1336–1343. https://doi.org/10.1016/j.pss.2006.04.018

Zhao, X., & Dryer, M. (2014). Current status of CME/shock arrival time prediction. *Space Weather*, *12*(7), 448–469. https://doi.org/10.1002/2014SW001060

Zhu, C., Alexander, D., Sun, X., & Daou, A. (2014). The role of interchange reconnection in facilitating a filament eruption. *Solar Physics*, *289*(12), 4533–4543. https://doi.org/10.1007/s11207-014-0592-9

Zhuang, B., Wang, Y., Shen, C., Liu, S., Wang, J., Pan, Z., et al. (2017). The significance of the influence of the CME deflection in interplanetary space on the CME arrival at Earth. *The Astrophysical Journal*, *845*(2), 117. https://doi.org/10.3847/1538-4357/aa7fc0

Zhukov, A. N., & Auchère, F. (2004). On the nature of EIT waves, EUV dimmings and their link to CMEs. *Astronomy & Astrophysics*, *427*, 705–716. https://doi.org/10.1051/0004-6361:20040351